THE ASTROPHYSICAL JOURNAL, 449:460–475, 1995 August 20

A METHOD FOR WEAK LENSING OBSERVATIONS

NICK KAISER,[1] GORDON SQUIRES,[2] AND TOM BROADHURST[3]

Received 1994 November 7; accepted 1995 January 31

ABSTRACT

We develop and test a method for measuring the gravitational lensing–induced distortion of faint background galaxies. We first describe how we locate the galaxies and measure two-component "polarization" or ellipticity statistic e_α whose expectation value should be proportional to the gravitational shear γ_α. We then show that an anisotropic instrumental point-spread function (PSF) perturbs the polarization by $\delta e_\alpha = P^s_{\alpha\beta} p_\beta$, where p_α is a measure of the PSF anisotropy and $P^s_{\alpha\beta}$ is the "linearized smear polarizability tensor." By estimating $P^s_{\alpha\beta}$ for each object we can determine p_α from the foreground stars and apply a correction $-P^s_{\alpha\beta} p_\beta$ to the galaxies. We test this procedure using deep high-resolution images from the *Hubble Space Telescope* (*HST*) which are smeared with an anisotropic PSF and then have noise added to simulate ground-based observations. We find that the procedure works very well. A similar analysis yields a linear shear polarizability tensor $P^\gamma_{\alpha\beta}$ which describes the response to a gravitational shear. This calibrates the polarization-shear relation, but only for galaxies which are well resolved. To empirically calibrate the effect of seeing on the smaller galaxies we artificially stretch *HST* images to simulate lensing and then degrade them as before. These experiments provide a rigorous and exacting test of the method under realistic conditions. They show that it is possible to remove the effect of instrumental PSF anisotropy and that the method provides an efficient and quantitative measurement of the gravitational shear.

Subject headings: cosmology: observations — dark matter — galaxies: formation — gravitational lensing — large-scale structure of universe

1. INTRODUCTION

Gravitational lensing of faint background galaxies provides a powerful probe of the mass distribution in and around clusters (Tyson, Valdes, & Wenk 1990; Miralda-Escude 1991a; Kochanek 1991; Bonnet et al. 1994; Bonnet & Mellier 1994; Mellier et al. 1994; Smail et al. 1994a, b; Fahlman et al. 1994; Dahle, Maddox, & Lilje 1994; Schneider & Seitz 1994; Seitz & Schneider 1994; Schramm & Kayser 1994; Broadhurst, Taylor, & Peacock 1994; Fort & Mellier 1994; Kaiser et al. 1994; Tyson 1995) and potentially of large-scale structure (Blandford et al. 1991; Miralda-Escude 1991b; Kaiser 1992; Mould et al. 1994; Gould & Villumsen 1994). Lensing will both amplify and distort the images of background galaxies. Here we will restrict attention to the statistical anisotropy of the background galaxies caused by the tidal shearing of the light rays.

With perfect seeing, the effect of a gravitational lens is a simple Lagrangian mapping of the surface brightness pattern

$$f'(\theta_i) = f(\psi_{ij}\theta_j)\,, \tag{1.1}$$

here f' is the observed surface brightness and f that which would have been observed in the absence of lensing and where angles are measured relative to some fiducial point on the image (e.g., the center). In the weak lensing regime—the main subject of this paper—the image shear tensor ψ_{ij} is close to the unit matrix, and $\psi_{ij} - \delta_{ij}$ is just an integral along the line of sight of the transverse components of the tidal field (e.g., Kaiser 1992). For the special case of a planar lens, $\psi_{ij} = \delta_{ij} - \phi_{ij}$, where the dimensionless *surface potential* ϕ is related to the projected mass density by Poisson's equation in two dimensions, $\nabla^2\phi = 2\Sigma/\Sigma_{\rm crit}$. For an Einstein–de Sitter universe the inverse critical surface density is $\Sigma^{-1}_{\rm crit} \equiv 4\pi a_l w_l \beta$, where w_l is the comoving distance to the lens, $w_l = 1 - (1 + z_l)^{-1/2}$, a_l is the scale factor at z_l, and the factor $\beta \equiv \max(0, 1 - w_l/w_s)$ gives the distortion strength as a function of the source distance w_s ($\beta \to 1$ for $w_s \gg w_l$).

For a spatially constant ψ_{ij} the mapping (eq. [1.1]) describes a simple anisotropic dilation of the images much as though the galaxies were painted on a rubber sheet which is then stretched. The ratio of the stretch factors along the axes in the diagonal frame (for an intrinsically circular object this is just the ratio of the major and minor axes) is equal to the ratio of the eigenvalues of the tensor ψ_{ij}. In reality we will see a superposition of source planes at different redshifts which will have been distorted by different amounts (though for cluster lenses at $z \lesssim 0.2$ the distribution of β values is actually quite narrow [see § 5], and the single sheet approximation is quite good). The goal of the research described here was to develop techniques to measure the mean anisotropy strength and orientation φ for the galaxies on some patch of sky; in the weak distortion regime ($\phi_{ij} \ll 1$) the distortion is proportional to the shear $\gamma_i \equiv \gamma\{\cos 2\varphi, \sin 2\varphi\}$, where $\gamma \equiv (\lambda_1 - \lambda_2)/2$, with λ_1, λ_2 being the eigenvalues of ϕ_{ij}. How the surface density Σ may be reconstructed from measurement of γ has been discussed in more detail elsewhere (Kaiser & Squires 1993, hereafter KS93; Kaiser et al. 1994; Schneider & Seitz 1994; Schneider 1994).

The distortion is locally specified by the two parameters γ, φ (or γ_1, γ_2). To detect this we follow the approach of Tyson et al. (1990): we identify faint galaxies and form from the trace free

[1] Canadian Institute for Advanced Research and Canadian Institute for Theoretical Astrophysics, University of Toronto, 60 St. George Street, Toronto, Ontario, Canada M5S 1A7; kaiser@cita.utoronto.ca.
[2] Physics Department, University of Toronto, 60 St. Georges Street, Toronto, Ontario, M5S 1A7; squires@cita.utoronto.ca.
[3] Astronomy Department, John Hopkins University, Baltimore, MD 21218; tjb@skysrv.pha.jhu.edu.

parts of the quadruple moments of their images a two-component entity that we call, following Blandford et al. 1991, the *polarization* e_i. The relation between e_α and galaxy shape is illustrated in Figure 1. The key feature of this statistic is that in the absence of lensing it averages to zero for statistically isotropic (i.e., randomly oriented) objects, but in the presence of lensing develops an expectation value that is proportional to the gravitational shear. There are many other ways one could detect this anisotropy, but the quadrupole moment method seems to be practical and has so far been used exclusively by all groups mentioned above (though with subtle differences in how the technique is actually implemented; see discussions of Kochanek 1991; Miralda-Escude 1991b; Bonnet & Mellier 1994).

In real observations there will also be artificial distortion of the images arising in the atmosphere and telescope. These effects are of two types. There may be a general distortion of the field arising in the optics of the telescope and/or CCD camera. This, like the gravitational effect, consists of a stretching of the image. This can easily be measured from the displacement of stellar images and can be corrected for. A more pernicious effect is the *smearing* of images with an anisotropic point-spread function (PSF). There are many possible sources of PSF anisotropy; some of these are discussed in Appendix C. The signals one is trying to measure are very small: typically a few percent in the outskirts of clusters and around 1% for large-scale structure. This kind of precision is possible in principle owing to the extremely large number of background galaxies over the scale on which the shear is coherent: typically thousands for clusters and potentially hundreds of thousands for large-scale structure. It is clearly vital that systematic effects of this kind, which can easily be comparable to or greater than the signal, be corrected for. As we shall see, this appears to be quite feasible due to the presence of foreground stars, which provide a control sample from which one can measure the PSF quite precisely.

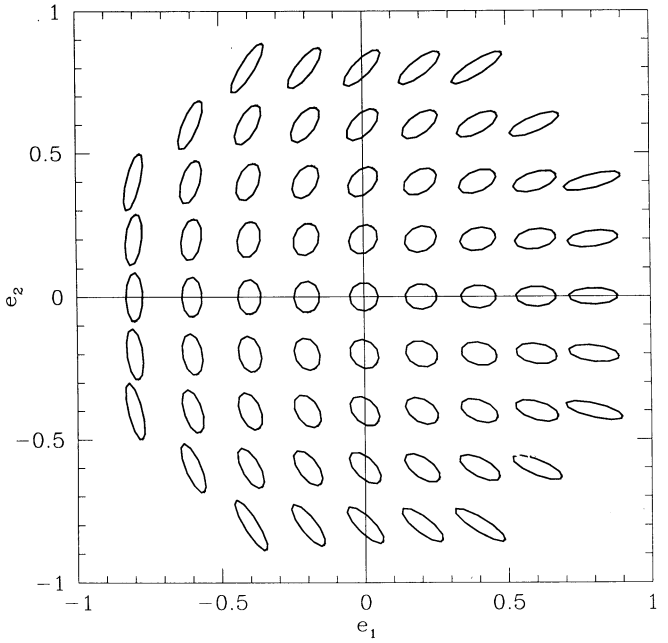

FIG. 1.—Polarization values for a family of Gaussian ellipsoid objects of varying degrees of polarization and orientation. The equal area ellipses are contours of surface brightness. The polarization values here are $e_1 = (Q_{11} - Q_{22})/(Q_{11} + Q_{22})$, $e_2 = 2Q_{12}/(Q_{11} + Q_{22})$, where Q_{ij} is a simple unweighted central second moment. For technical reasons we actually use a weighted moment, but at a qualitative level, the relation between shape and polarization values is as shown here.

Over the past few years we have developed software which measures the statistical anisotropy of faint galaxies, and we have applied this with some success to a number of clusters. The purpose of this paper is to describe the procedure in some detail, and in one place, and to demonstrate that the techniques actually work (though they may not yet be optimal). The logical order of the paper follows the steps in the analysis of actual CCD images. In § 2 we describe the object detection algorithm, and in § 3 we describe the galaxy photometry and shape analysis algorithms. In § 4 we describe how we can remove the effect of PSF anisotropy, and finally, in § 5 we describe how we quantify the shear. All of the steps are illustrated with real images, and in §§ 4 and 5 we use deep *Hubble Space Telescope* (*HST*) images which are smeared and stretched to simulate the effect of the atmosphere, PSF anisotropy, and gravitational lensing. These images are then further degraded with noise to the same level as our typical ground-based data and are then analyzed in exactly the same manner. These experiments clearly demonstrate that we can measure and remove the effect of any PSF anisotropy with high precision, and they give a direct calibration of the effect of seeing which previously required some modeling of the unknown sizes and shapes of these faint and typically poorly resolved objects.

2. OBJECT DETECTION

Our method for detecting faint objects is very simple and consists in essence of smoothing the images and locating peaks. This is rather different from, e.g., the Faint Object Classification and Analysis System (FOCAS) approach (Jarvis & Tyson 1981), which locates connected regions which lie above a threshold, but is similar to some other detection schemes (Kron 1980; Yee 1991).

Our first attempts used a single fixed smoothing filter with radius somewhat larger than the seeing disk; this is also the strategy adopted by Bonnet & Mellier (1994). We experimented with various shapes for the kernel and opted for a simple Gaussian (Bonnet & Mellier use a "Mexican hat" filter). Our algorithm has subsequently evolved, motivated in part by considerations of a simple model in which one has Gaussian ellipsoid objects (plus noise) whose axial ratios and orientations one wishes to measure by means of Gaussian window–weighted quadrupole moments. It turns out that for a single isolated object of this kind, the optimum scale for the filter is just equal to the object's post-seeing scale length. We also found that the signal-to-noise ratio (S/N) was very sensitive to the choice of smoothing radius, so it seems desirable that our object detector should provide some reasonable estimate of the object size to which we can tune our shape measurement window function. Now for Gaussian ellipsoids, the same filter radius is also optimal for detecting the object (i.e., the S/N for the peak is greatest when viewed at this resolution), so if one smooths an image with all possible smoothing radii and then chooses the peak of greatest significance, this will provide both the position and the optimal filter radius for the object. The significance here is defined to be $\nu = \mathrm{S/N} = \propto f_s r_f$, where f_s is the smoothed peak surface brightness and r_f is the filter radius. Real galaxies are not Gaussian of course, but the sensitivity of S/N to the choice of weighting function is

probably a general feature, and the hope is that the scale size determined in this way can be used to improve the precision of our shape estimation.

We have implemented such an algorithm on the computer. We smooth the image with a range of filters, typically with steps in log filter radius of $\delta \ln r_f = 0.2$, find the peaks of the smoothed images, and then link these together and construct a catalog of peak trajectories. The behavior of these trajectories is illustrated in one dimension in Figure 2. We initially used a simple Gaussian smoothing kernel but found that this missed some faint objects with bright neighbors, and we now use a compensated "Mexican hat" style filter, though we have not explored the possibilities here in great detail.

The behavior of the object finder in two dimensions is shown in Figure 3 (Plate 9). The raw catalog produced by the hierarchical peak finder was initially filtered with a low significance threshold (3 σ), and contained, in addition to the real objects, a large number of unwanted noise peaks and some groups of galaxies. We have found that an effective way to clean up the catalog is to split the image data into two subsets (usually we have some large number of images) and combine these to form two images of the same patch of sky, but with statistically independent noise properties. Each combined image has a slightly lower S/N than would be obtained from the complete data set, but by setting a low threshold we find we can still recover a high density of objects. We can then remove cosmic rays and noise peaks, etc., by applying a spatial coincidence test. In the example shown in Figure 3 we require that the positions should coincide to within 2 pixels. This effectively removes the larger groups, as their positions tend to be more uncertain than this, and also removes essentially all of the noise peaks. Once we have pruned our object catalog in this way, we can of course perform the photometric analysis of the objects using an image formed from all the data (or simply average the properties of the catalogs from the individual data sets).

We find the visual appearance of the final catalog in Figure 3 quite encouraging. The algorithm has detected essentially all of the objects of any significance and seems to have assigned sensible scale sizes. Our earlier attempts at object finding with a fixed smoothing filter produced, in addition to most of the real objects, a large number of false detections sitting on the

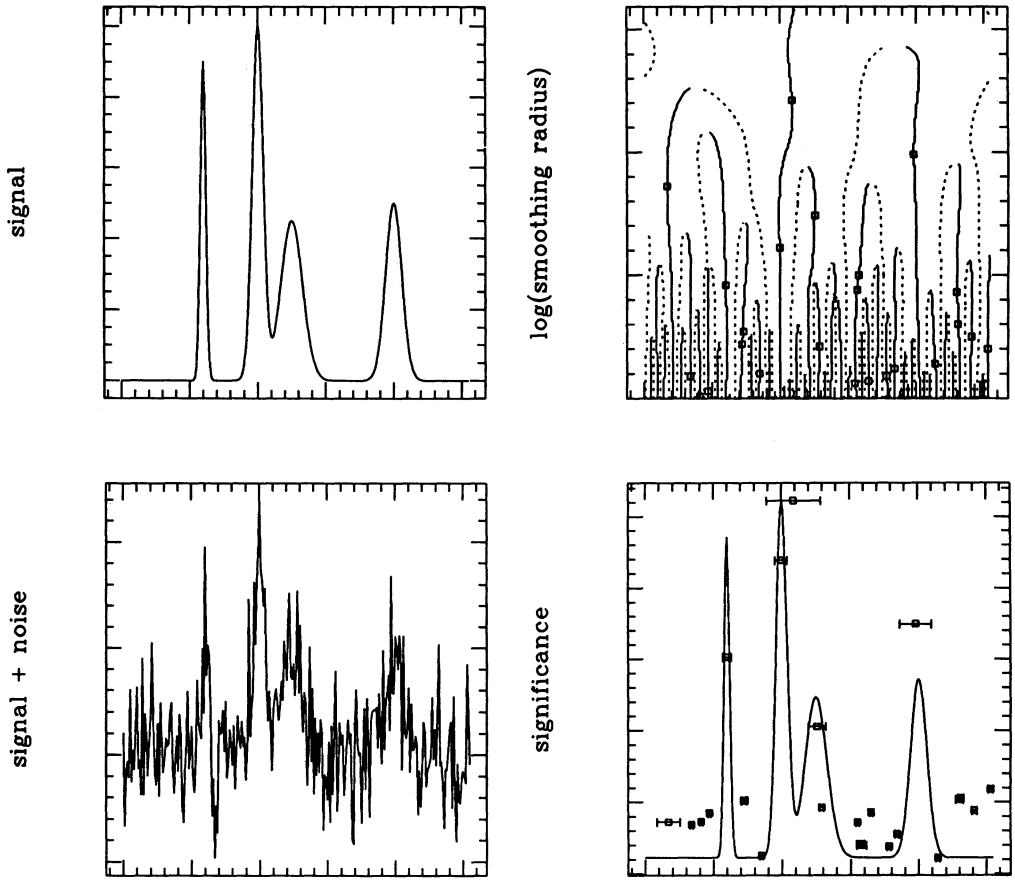

FIG. 2.—Peak trajectories for one-dimensional model image consisting of a number of Gaussian profile objects of varying sizes and central surface brightness. The model image is shown with and without noise on the left, and the upper right panel shows the peak trajectories as a function of smoothing radius (vertical scale). Solid and dotted lines show maxima and minima, and the squares show the local maxima of the significance. This shows the generic behavior of peaks in one dimension; at small smoothing radius we have a large number of (mainly noise) peaks, but these gradually annihilate with minima (where the smoothed image has an inflection point). In two dimensions, peaks annihilate with saddle points. In the lower right panel we show the local significance maxima, where the vertical scale is now the significance level, and the width of the symbol denotes the smoothing radius. The original model image is shown superposed for comparison. There is a clear gap between the noise peaks and the real objects. The algorithm has detected all four real objects and has assigned reasonable values for their radii. It has also detected the central pair of objects as a significant object in its own right, and similarly in two dimensions we find that our "hierarchical peak finder" finds pairs and groups of galaxies as well as individual galaxies. Such composite objects can easily be removed from the final catalog if desired.

diffuse light around bright stars and foreground galaxies, and these had to be manually edited from the catalog. In the near future we anticipate gathering much larger images using large-format CCD mosaics (e.g., Cuillandre et al. 1994; Luppino, Bredthauer, & Geary 1994), and having a nearly automated data reduction pathway from image to usable catalog will obviously be a great practical advantage. The algorithm is, aside from the choice of smoothing window shape, entirely parameter free. Finally, we mention that any detection algorithm like this which uses a circularly symmetric smoothing kernel will be biased in the shapes of the faintest objects, as a circular object will be more easily detected than an elongated one. As we shall see, this does not seem to cause serious problems.

3. OBJECT ANALYSIS

Armed with a catalog of object positions we now determine a number of shape, luminosity, etc., parameters. Quite often we find that the preliminary data reduction leaves some unwanted low-level low spatial frequency variations in the sky background. This does not seriously affect the object detection phase, as we use a compensated filter, but can have an effect on the shapes. If we find such problems we instruct the analysis software to perform a local modeling of the sky background level. This is illustrated in Figure 4 (Plate 10). Having corrected the pixel values, we are now ready to estimate basic photometric parameters and shapes.

3.1. *Basic Photometry*

The object finder already provides a crude estimate of the radius and luminosity of the objects. To determine a better half-light radius, which we use for star/galaxy separation, and "total" magnitude we proceed as follows. Using the surface brightness corrected for the local background, we calculate the growth curve for the integrated light $I(<r) \equiv 2\pi \int d\theta\, \theta f(\theta)$ [where $f(\theta)$ denotes the surface brightness] as a function of radius and determine a half-light radius and total luminosity within an aperture. We have experimented with different types of apertures. We currently favor an aperture of 3 times the scale length returned by the object finder; these are the circles drawn in Figure 3. We have also used an alternative which is 3 times the Petrosian radius [this is the radius where $I(<r)/r$ peaks], the factor 3 in both cases being chosen as subjective compromise between obtaining a "true" total magnitude and precision. The aperture radii are generally very similar, but for some of the objects the Petrosian radius estimator appears unreliable. Examples of the results of the basic photometric analysis are shown in Figure 5.

3.2. *Shape Estimation*

The shape parameters we use are formed from weighted quadrupole moments,

$$Q_{ij} \equiv \int d^2\theta W(\theta)\theta_i\theta_j f(\theta)\,, \tag{3.1}$$

where angles are measured relative to the object position as determined in the detection phase. We take $W(\theta)$ to be a Gaussian with scale length equal to some multiple of the scale determined in the object detection phase. Currently, we use a multiplier of unity, as this seems from experimentation to be a good choice—with more extensive *HST* data and experiments of the kind performed below it should be possible to optimize this parameter.

We then define the polarization parameters by

$$e_\alpha \equiv Q_\alpha/T\,, \tag{3.2}$$

with

$$Q_1 \equiv Q_{11} - Q_{22}\,, \quad Q_2 \equiv 2Q_{21}\,, \quad T \equiv Q_{11} + Q_{22}\,, \tag{3.3}$$

which clearly provides some measure of the ellipticity of an object: $e_\alpha = 0$ for a circularly symmetric object. Now under a rotation of the coordinate frame $e_\alpha \to R_{\alpha\beta}(2\varphi)e_\beta$, where R is the two-dimensional rotation matrix, so, in the absence of lensing, the polarization values will be isotropically distributed about the origin on the e_1, e_2 plane. In the case of unweighted moments ($W = 1$), it is easy to see how these statistics will be perturbed by a gravitational shear, since the mapping $f(\theta) \to f(\psi \cdot \theta)$ simply corresponds, in the diagonal frame, to a rescaling of the coordinate axes so $Q'_{ij} = Q_{ij}/\Lambda_1\Lambda_2\,\Lambda_i\Lambda_j$, or, in the weak shear limit, $Q'_{ij} = Q_{ij}(1 - [\lambda_1 + \lambda_2 + \lambda_i + \lambda_j])$, where as before primed and unprimed quantities denote the perturbed and unperturbed values, respectively. For isotropic objects $\langle Q_1\rangle = 0$, but in the presence of shear there will be a systematic shift in $\langle Q'_1\rangle$ proportional to $\lambda_1 - \lambda_2 = \gamma$. The way we have chosen to normalize the moments (to unit trace), the shift in the polarization due to a given shear depends to a slight extent on the polarization of the object (and so the shift in the mean polarization depends somewhat on the distribution of ellipticities). Bonnet & Mellier(1994) have made the interesting suggestion that one normalize to unit determinant. The shift in the polarization is then independent of the intrinsic ellipticity; in fact, the mean shift is just $\langle \delta e_\alpha\rangle = 2\gamma_\alpha$. This simple relation between δe and γ is a nice property, but unfortunately this does not hold for weighted moments (and unweighted second moments are impractical owing to divergent noise). With weighted moments and with either normalization scheme, the shift depends in a nontrivial way on the intrinsic shapes distribution, but, as we will see, this does not present an insurmountable problem.

If one ignores, for the moment, the effects of seeing and photon counting noise, it is fairly straightforward to calculate how the polarization parameters will change under a constant (and small) gravitational shear for an arbitrary window function $W(\theta)$. As we show below, the first-order change in polarization induced by the shear can be written as

$$\delta e_\alpha = P^\gamma_{\alpha\beta}\gamma_\beta\,, \tag{3.4}$$

where $P^\gamma_{\alpha\beta}$ defines the *shear polarizability tensor*. Note that, strictly speaking, $P^\gamma_{\alpha\beta}$ is not a tensor: e_α and γ_α are two-component entitites, but they are not vectors, as they transform under rotations as $e_\alpha \to R_{\alpha\beta}(2\theta)e_\beta$. Similarly, our polarizabilities transform as $P_{\alpha\beta} \to R_{\alpha\gamma}(2\theta)P_{\gamma\delta}R^{-1}_{\delta\beta}(2\theta)$. We will henceforth sloppily refer to these objects as tensors and vectors, but we try to distinguish them by using Greek symbols for their indices and using latin indices for real vectors and tensors.

Now $P^\gamma_{\alpha\beta}$ is some rather messy combination of angular moments of the surface brightness, but the important point is that it can be directly measured for each individual galaxy image and so provides a way to calibrate the polarization statistics: the average of $e_\beta/P^\gamma_{\alpha\beta}$ over the galaxies lying on some patch of sky is just proportional to the shear γ_α averaged over

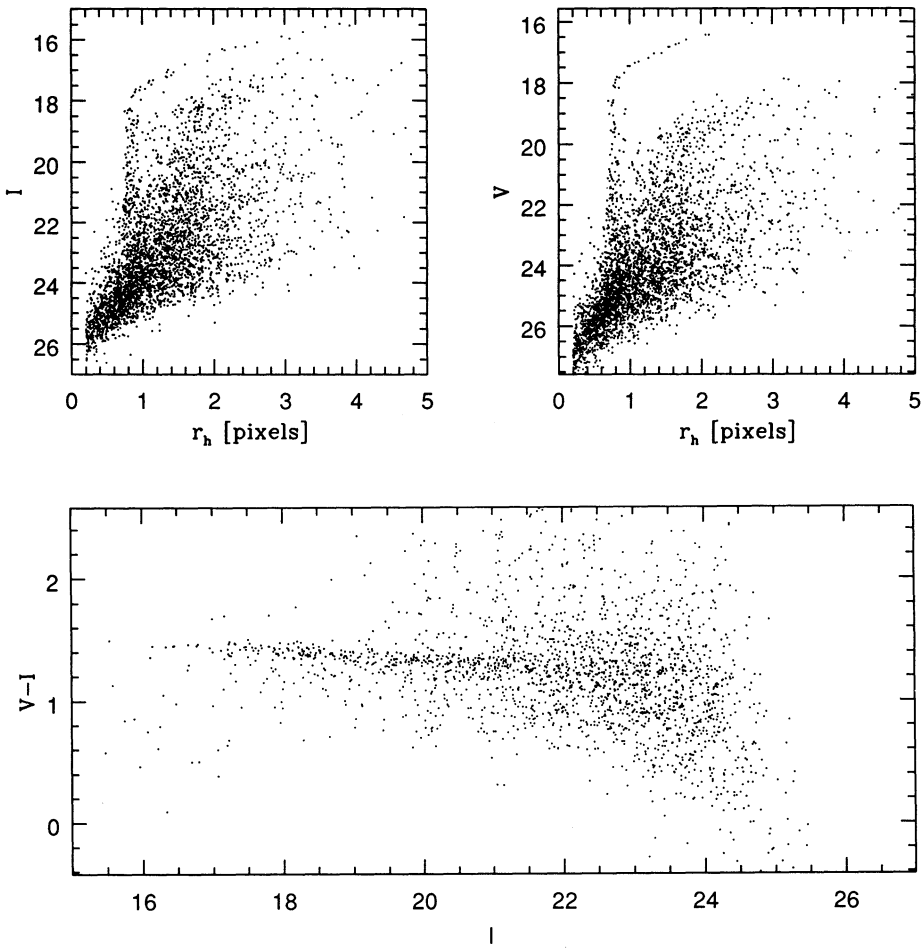

FIG. 5.—Upper panels show half-light radii and magnitudes determined from typical ground-based observations. The data here were taken at the NTT, with 0".7 seeing and 0".34 pixels. The vertical stellar locus is clearly seen, and it is possible to separate moderately bright stars from galaxies with confidence—this is vital for measuring and correcting for point-spread function (PSF) anisotropy. The bright stars are saturated and consequently swell up, but the transition seems quite sharp and it appears to be quite easy to select a sample of moderately bright stars with which one can reliably measure the PSF. The lower panel shows the color magnitude diagram for extended objects; the cluster (A1689) sequence is very sharply delineated.

the same region. In this way we can always construct a statistic which gives an unbiased estimate of the shear. Now noise in the image will mean that we make some error in calculating $P^{\gamma}_{\alpha\beta}$, but, as we will see, this does not seem to be a serious problem. A bigger problem comes from seeing, which will perturb both the polarization and the polarizability in a systematic way. The approach we have adopted is a semiempirical one: We first calculate as best we can the polarizability ignoring seeing—this should provide a set of shear estimates which have a negative bias which depends on the image size but which should asymptote to the correct value for large images—and we then empirically calibrate the seeing-induced suppression as a function of image size by using *HST* data which we artificially stretch and then degrade to simulate ground-based observing conditions. The technical details of this are given below (§ 5).

First, however, we will address a closely related problem: how the mean polarization shifts in response to smearing with an anisotropic PSF, and how we can, by measuring the PSF of foreground stars, annul this. Provided the PSF is close to circular—and this fortunately seems to be the case for the data at which we have looked—we can define a linearized "smear polarizability" such that

$$\delta e_{\alpha} = P^{s}_{\alpha\beta} p_{\beta} , \tag{3.5}$$

where p_{β} is some measure of the PSF anisotropy. The smear polarizability can, like $P^{\gamma}_{\alpha\beta}$, be calculated for each object. The nice thing here is that $P^{s}_{\alpha\beta}$ depends only on the image shape *after* seeing and so can be calculated exactly, in the absence of noise, and seems to be a rather robust statistic even in the presence of noise for our faint galaxies. The bulk of the rest of the paper is devoted to the calculation of these polarizability tensors and to a description of experiments with the *HST* observations to show how they work under realistic conditions with noise, finite pixel size, crowding of neighboring images, etc.

4. CORRECTION FOR PSF ANISOTROPY

A number of sources of PSF anisotropy are discussed briefly in Appendix C. Most of these produce an anisotropy which is constant across a CCD frame or varies in a smooth manner. Provided that one has a sufficient number of foreground stars—and they must be not so bright that their shapes are distorted by nonlinearity in the CCD or readout electronics

—one can map the PSF anisotropy. One way to correct would be to reconvolve the image with an artificial PSF designed to give a circular final PSF, but this involves some loss of information. The approach developed here is to calculate how the polarization values of the galaxies respond to a given PSF anisotropy and apply an appropriate correction. We first present the analysis and then demonstrate the procedure with realistic test data.

4.1. *Analysis*

As we show in Appendix A, one can model any source of PSF anisotropy as a convolution of a circularly smeared image with a small, but highly anisotropic kernel $g(\boldsymbol{\theta})$ [in many cases this is just a small unidirectional smearing: $g(x, y) = \delta(x)g'(y)$ with some boxcar like function g']. For small PSF anisotropy, the shift in the polarization e_α depends only on $p_\alpha \equiv \{q_{11} - q_{22}, 2q_{12}\}$, where

$$q_{lm} \equiv \int d^2\theta \theta_l \theta_m g(\boldsymbol{\theta}) \tag{4.1}$$

is the unweighted quadrupole moment of g, and we have assumed that g is normalized such that $\int d^2\theta g = 1$ and that the origin of coordinates is chosen so that $\int d^2\theta \theta_i g(\boldsymbol{\theta}) = 0$. The perturbation to the polarization is, to linear order in p_α,

$$\delta e_\alpha = P^s_{\alpha\beta} p_\beta \,, \tag{4.2}$$

where the smear polarizability tensor is

$$P^s_{\alpha\beta} = X^s_{\alpha\beta} - e_\alpha e^s_\beta \,, \tag{4.3}$$

where

$$X^s_{\alpha\beta} = \frac{1}{T}\int d^2\theta \times \begin{bmatrix} 2W + 4W'\theta^2 + 2W''(\theta_1^2 - \theta_2^2)^2 & 4W''(\theta_1^2 - \theta_2^2)\theta_1\theta_2 \\ 4W''(\theta_1^2 - \theta_2^2)\theta_1\theta_2 & 2W + 4W'\theta^2 + 8W''\theta_1^2\theta_2^2 \end{bmatrix} f(\boldsymbol{\theta}) \,, \tag{4.4}$$

$$e^s_\alpha \equiv \frac{1}{T}\int d^2\theta \begin{pmatrix} \theta_1^2 - \theta_2^2 \\ 2\theta_1\theta_2 \end{pmatrix} (6W' + 2W''\theta^2) f(\boldsymbol{\theta}) \,, \tag{4.5}$$

and where prime denotes differentiation with respect to θ^2. The surface brightness here is that after any circularly symmetric seeing, which to zeroth order in p_α is just the observed surface brightness. Note that for the impractical case of an unweighted quadrupole moment ($W' = W'' = 0$) the smear polarizability is diagonal with $P^s_{11} = P^s_{22} = \int d^2\theta f / \int d^2\theta \theta^2 f = \langle\theta^2\rangle^{-1}$ independent of the intrinsic ellipticity distribution. This would not be the case were we to normalize to unit determinant. Note also that $P^s_{\alpha\beta}$ is diagonal for any circular object such as a star.

We can measure the shear polarizability for each individual object. The stars then provide an estimate of $p_\alpha = e_\alpha / P^s_{\alpha\alpha}$ (no summation), and we can correct each galaxy polarization by an amount $-P^s_{\alpha\beta} p_\beta$ and restore the polarization values to what would have been seen with a perfectly isotropic PSF. All this assumes noise-free data. The stars are reasonably bright, so photon counting noise is little problem there. The polarizabilities estimated for the galaxies will be much noisier, and this introduces both a random and systematic error in $P^s_{\alpha\beta}$. The random error is relatively benign, since our goal is to finally determine a shift in the mean polarization. The systematic error arises in the second term in $P^s_{\alpha\beta}$ which is quadratic in the surface brightness, so for very faint objects this will introduce a bias, as the observed $e_\alpha e^s_\alpha$ will be inflated by photon counting noise. One could easily calculate the size of this effect and apply an appropriate correction, but in fact the second term tends to be quite small, and we have not done so.

For the correction procedure to work it is vital that one has sufficiently many stars to sample any variation of the PSF anisotropy across the chip. In the case of the NTT data shown in Figure 3 we obtained a subsample of about 30 stars (on $\simeq 70$ square arcmin) which were sufficiently bright that they can be distinguished from galaxies with near certainty, yet not so bright that they are saturated. As discussed in Appendix C, most anticipated effects will produce a slowly varying anisotropy, so the number of stars should be adequate. In a typical observing run we end up with some number of fields (each formed by averaging several images with rejection of outliers). From the subsample of stellar objects our software currently attempts to fit a model in which there is a spatially constant anisotropy $\bar{p}_\alpha$ for each field (this should accurately describe influences such as wind shake and atmospheric dispersion) and a "global" low-order polynomial in angle on the chip which should accommodate any reproducible aberration effects. The software starts with a zeroth-order fit and then increments the order of the fit while monitoring the residuals. As an example, for the Fahlman et al. (1994) data we found a significant linear gradient but no significant improvement in fit was obtained for higher order fits, so we used the linear model.

4.2. *An Experiment with Hubble Space Telescope Data*

The expression (4.3) for the smear polarizability is rather involved, to say the least, so it is difficult to analytically quantify the uncertainty and the various biases present in the PSF correction process. One way to rigorously test the procedure is to take very deep images and convolve them with a small but highly anisotropic PSF so that the total PSF develops a small anisotropy. We can then add noise to the level in our typical integrations and analyze the images, separate and measure the polarizations of the stars, and then apply the appropriate correction. We can then see how well the correction works in a realistic situation. It is necessary that we start with very long integrations, however, since we would otherwise be smearing any noise in the original image, which would be unrealistic.

It turns out that *HST* data are very useful here. While the aperture of the telescope is relatively small, the sky is so much fainter for *HST* (about 2.5 mag in the *I* band) that one can go very deep in integrations of reasonable length. The data we will use here are ~ 2 hr WFPC2 integration on a single target. This gives us three CCD frames, each 1.'25 square. Part of one of these is shown in Figure 6 (Plate 11). The rms level of the noise added was about twice that in the rebinned (but unsmoothed) *HST* data, so the noise from the original image should be negligible. The limiting magnitude in the degraded images is very similar to that in the NNT data shown above. The total area is 5 square arcmin, yielding a few hundred detectable galaxies.

A further advantage of using *HST* data is that it allows one to address the question of "pixelization." The expresssions for the smear polarizability, etc., are all expressed as integrals of continuous functions, whereas in reality they are implemented

as discrete sums over pixels. The 0.″1 WFPC2 pixels are much smaller than the pixels in the rebinned images, so any effect arising from the finite pixel size in the ground-based observations should be seen in the simulations.

To test the PSF anisotropy correction machinery we have degraded these data much as shown in Figure 6, but with an anisotropic PSF: a Gaussian ellipsoid with $a/b \simeq 2$ and with the same area as the PSF used in Figure 6. In an attempt to boost the statistical signal somewhat, we have smeared the images in four ways with PSF position angles 0°, 45°, 90°, 135° degrees, and we have used two independent realizations of noise, though the results are not really statistically independent. The PSF–induced polarization is clearly seen in the upper left-hand panel of Figure 7 (for each frame we have applied the rotation matrix $R_{\alpha\beta}(2\varphi)$ to the e_α estimates so that the θ_1 direction lies along the stellar major axis). There is considerable "cosmic variance" in this plot due to the random intrinsic ellipticities of the relatively small number of real galaxies used. We can get a somewhat cleaner picture of the shift if we pair up objects found from the anisotropically smeared images with those found with circular seeing and plot the *change* in the polarization values δe_α introduced by the PSF anisotropy. This is shown in the upper right-hand panel. The lower panels in Figure 7 show that the induced ellipticity shift is primarily a function of the image size, being greatest for the smallest images as expected, and has a rather weak dependence on luminosity. Figure 8 shows the same plots, but after measuring the shear from the actual stellar images and applying the correction as described. Clearly, the procedure has worked very well indeed, and any residual anisotropy is very small.

There is a hint that the method may overcorrect the faintest galaxies. The catalogs used here were limited to 5 σ detections and above. If one includes even lower significance detections, then the overcorrection appears to be stronger. Perhaps this is because we are seeing the bias toward circular objects at very low significance level. There might also be some residual arising from departures from linearity, as the PSF was so strongly anisotropic, but the limited numbers of galaxies here do not allow us to measure this with any precision.

The issue of PSF anisotropy correction has been considered by Bonnet & Mellier (1994) and by Mould et al. 1994, but both groups have derived a correction different from ours. Bonnet & Mellier (1994) treat the effect of PSF anisotropy as though it were a stretching of the images rather than a smearing. The correction that they apply is then independent of the image size. It is intuitively reasonable that a smearing (unlike a stretching) will produce an image polarization which scales in inverse proportion to the *area* of the image, and this is revealed quantitatively in our analysis: one can see on dimensional grounds that the smear polarizability defined by equations 4.3,

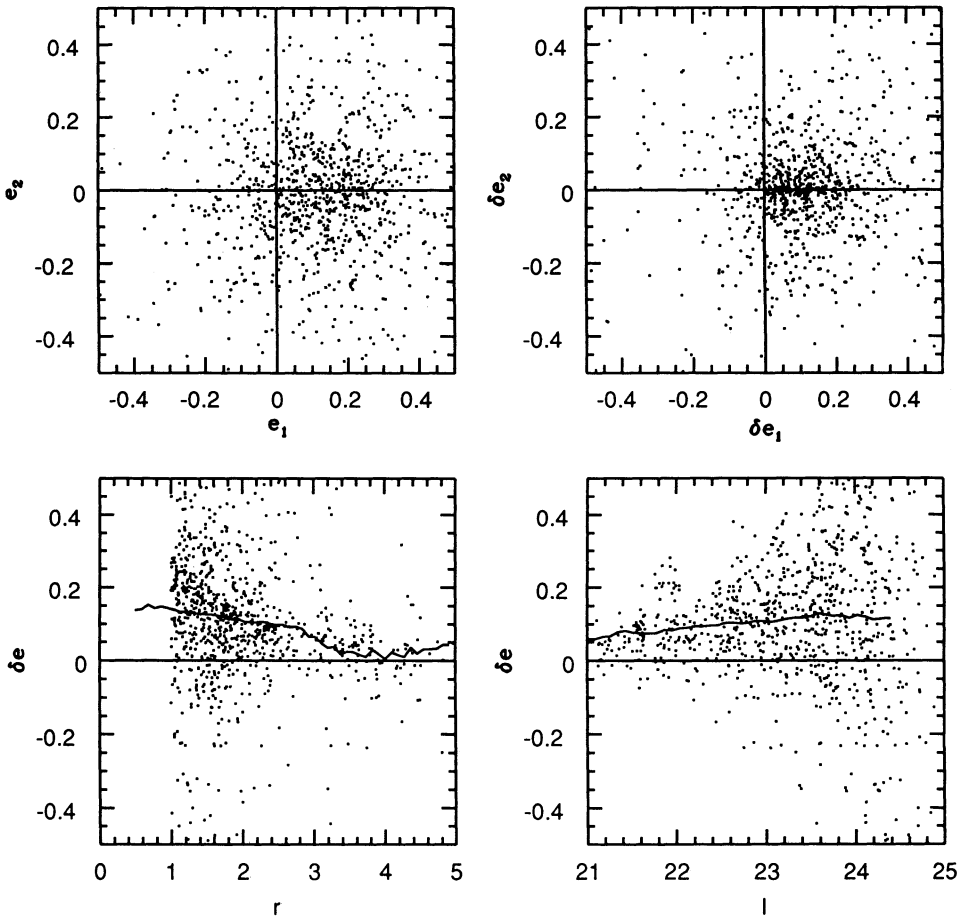

FIG. 7.—Upper left-hand panel shows the polarization values for images smeared with an anisotropic PSF. Upper right-hand panel shows the changes in polarization for smeared/unsmeared pairs of images. Lower panels show the dependence of the polarization shift on radius and apparent magnitude. The solid line is a simple moving average. The expected inverse trend with image size is clearly seen.

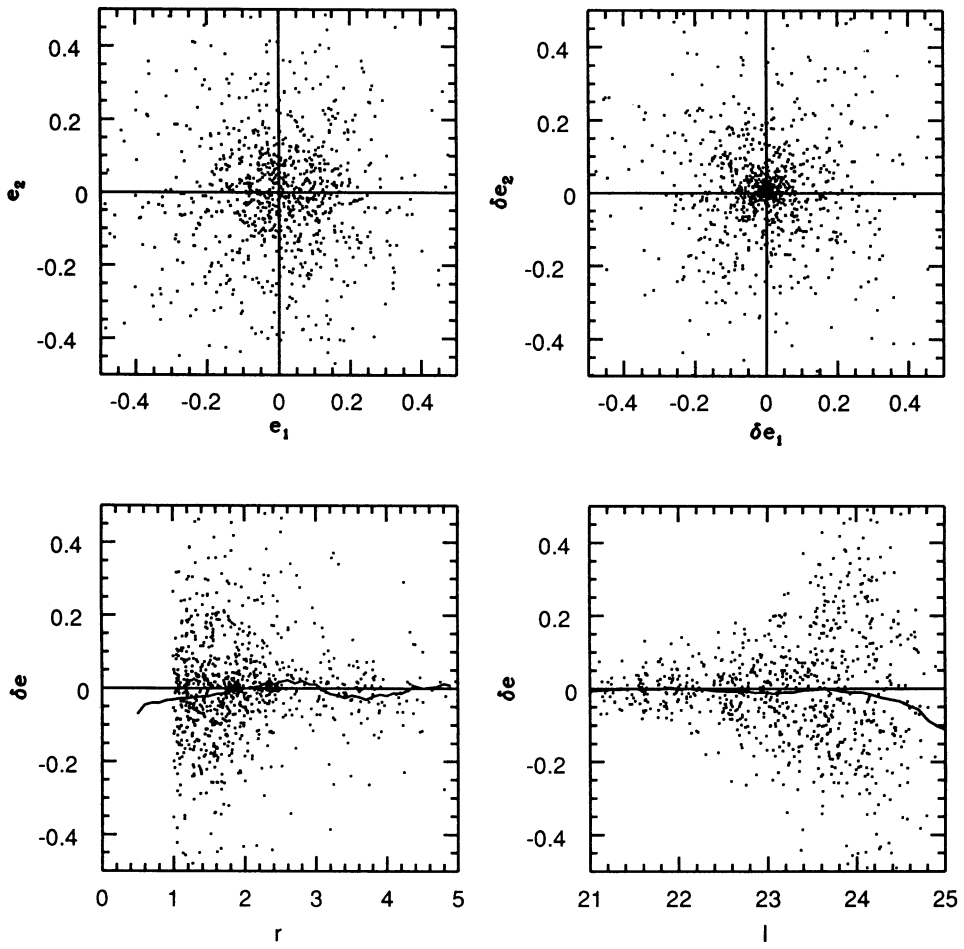

FIG. 8.—Polarization and polarization shift distributions after correction for PSF anisotropy as described in the text. The degraded *HST* data were analyzed in exactly the same way we analyze the real ground-based data, so this provides a rigorous and exacting test of the method, which it seems to have passed very well. If we average over a two-magnitude range as we typically do with the real data, then any residuals are less than about 10% of the uncorrected induced polarization. There is a hint that the method may overcorrect the faintest objects, but more data are needed to establish if this is a real effect.

4.4, 4.5 is a measure of the inverse area of the image, and the strong dependence of PSF-induced polarization on image size is shown graphically in Figure 7. As the Bonnet & Mellier (1994) correction is designed to cancel any anisotropy in the stars, we would expect that the result will be to overcorrect the galaxy polarizations. We would certainly make a serious error were we to apply a constant correction, but the kernel that Bonnet & Mellier (1994) use is rather different from ours, and so one would have to redo the analysis described above in order to quantify the error. Mould et al. (1994) argue that the effect of a PSF anisotropy will be a polarization which is inversely proportional to the linear size of the images rather than the area, as we find here. They were using the FOCAS software, which measures the second moments within an isophotal aperture which may behave differently from the weighted moments we use, but we suspect their procedure also overcorrects the galaxies.

It is interesting to ask, which is the dominant source of noise in the mean polarization, the $\sim e_{\rm rms}/\sqrt{N}$ fluctuations arising from the random intrinsic galaxy ellipticities and measurement error averaged over a large number of background galaxies, or the error feeding through from any error on the PSF anisotropy, which is determined from a small number of stars? It is difficult to give a definitive answer to this question, as it depends on how large the systematic PSF anisotropy one is trying to correct is, but our experience is that the dominant source of noise in the final error budget comes from the intrinsic variance in galaxy shapes. Note that if one is taking large numbers of images to get high S/N on a particular target lens, then any stochastic PSF anisotropy will tend to average away, and systematic effects should be removable in principle by, e.g., rotating the CCD by $\pi/2$ between pairs of images taken under identical conditions, and the noise from the random intrinsic ellipticities must, under such conditions, eventually come to dominate.

5. MEASURING THE SHEAR

Having removed the effect of PSF anisotropy, we are now ready to extract a quantitative estimate of the shear. As we show in Appendix B, if the galaxies are well resolved, it is relatively straightforward to calculate how the polarization values are perturbed by a gravitational shear. Much as in § 4, we obtain a linear response

$$\delta e_\alpha = P^\gamma_{\alpha\beta}\gamma_\beta\,, \tag{5.1}$$

but now with

$$P^{\gamma}_{\alpha\beta} = X^{\gamma}_{\alpha\beta} - e_\alpha e^{\gamma}_\beta \,, \tag{5.2}$$

with

$$X^{\gamma}_{\alpha\beta} = \frac{1}{T} \times \int d^2\theta \begin{bmatrix} 2W\theta^2 + 2W'(\theta_1^2 - \theta_2^2)^2 & 4W'(\theta_1^2 - \theta_2^2)\theta_1\theta_2 \\ 4W'(\theta_1^2 - \theta_2^2)\theta_1\theta_2 & 2W\theta^2 + 8W'\theta_1^2\theta_2^2 \end{bmatrix} f(\boldsymbol{\theta}) \,, \tag{5.3}$$

and with

$$e^{\gamma}_\alpha = 4e_\alpha + \frac{2}{T}\int d^2\theta \begin{pmatrix} \theta_1^2 - \theta_2^2 \\ 2\theta_1\theta_2 \end{pmatrix} \theta^2 W' f(\boldsymbol{\theta}) \,, \tag{5.4}$$

where prime denotes differentiation with respect to θ^2. For the impractical but simple case of constant weight we find $P^{\gamma}_{\alpha\beta} = 2(\delta_{\alpha\beta} - e_\alpha e_\beta)$ and $\langle P^{\gamma}_{\alpha\beta}\rangle = 2\delta_{\alpha\beta}(1 - \langle e_\alpha e_\alpha\rangle)$.

A fair estimate of the shear γ_α is therefore given by taking the mean of $e_\alpha P^{\gamma\,-1}_{\alpha\beta}$, the shear polarizability effectively providing a shape-dependent calibration factor. Unfortunately, all this ignores seeing which will dilute the polarization and also modify the polarizability tensor, and calculating the appropriate correction requires knowledge of the pre-seeing galaxy shape. The approach we have adopted in the past is as follows. We first calculate the shear polarizability and estimate γ_α as above. This will underestimate the true shear but should at least approach asymptotically to the correct value for large galaxies. We then empirically determine a correction as a function of galaxy size. In Fahlman et al., (1994) we estimated the correction under the assumption that the faint galaxies are scaled-down replicas of their brighter (and better resolved) cousins. Here we make a more direct estimation by taking *HST* data, shearing them, and then degrading them to simulate terrestrial observing conditions.

An alternative would be simply to develop an empirical calibration of the shear/polarization relation without trying to calculate the shear polarizability. This might actually improve the precision of the shear estimate because there appears to be a rather narrow distribution of shear polarizabilities (this is not surprising because P^{γ} depends only on the shape of the galaxies, unlike P^{s}, which is an inverse measure of the area of the image and so varies considerably from object to object), and the P^{γ} values are rather noisy. Thus, when we divide by the shear polarizability we may make a relatively large error in what should really be a small correction. From the experiments here it appears that the precision is very similar for these two methods, so more extensive experiments are required to see which is optimal.

5.1. *Empirical Calibration of the Effect of Seeing*

To empirically calibrate the shear estimator with finite seeing we used the same WFPC2 data as in § 4.2. These images were stretched to simulate the effect of lensing, as shown in Figure 10 (Plate 12). We then smeared these with a circular Gaussian PSF to simulate seeing, rebinned the images to a pixel scale appropriate for ground-based observations, and added multiple realizations of noise. We then applied the object-finding algorithm with coincidence testing as described in § 2. This experiment is arguably somewhat unrealistic in that we apply a constant stretch to all of the objects, whereas in reality we have a superposition of source "screens" each being smeared by a different amount. As the goal here is simply to determine a calibration factor for the shift in the mean polarization, this should not be much of a problem, and in any case, for cluster lenses at the redshifts we currently target ($z \lesssim 0.2$), and for reasonable magnitude limits to define the faint galaxy subsample, the constant shear approximation is quite good, as we show in Figure 9.

As a test of the shear-polarizability calculation, we then analyzed the objects found under realistic conditions, but using the unsmeared (but stretched) images. The result is shown in Figure 11. The image anisotropy is clearly seen, and calibration seems to have recovered the correct amplitude as expected. We now repeat the shapes calculation but using the stretched, smeared and noise-added images (Figs. 12 and 13). The expected dilution of the signal (primarily a function of image size) is clearly seen. With more extensive data it should be possible to calibrate this effect and quantify the trend with image size quite accurately. The experiment should give at least a reasonably secure overall calibration factor for any particular observation.

As well as showing the trend of mean polarization with image size, Figures 12 and 13 also shows empirically how the

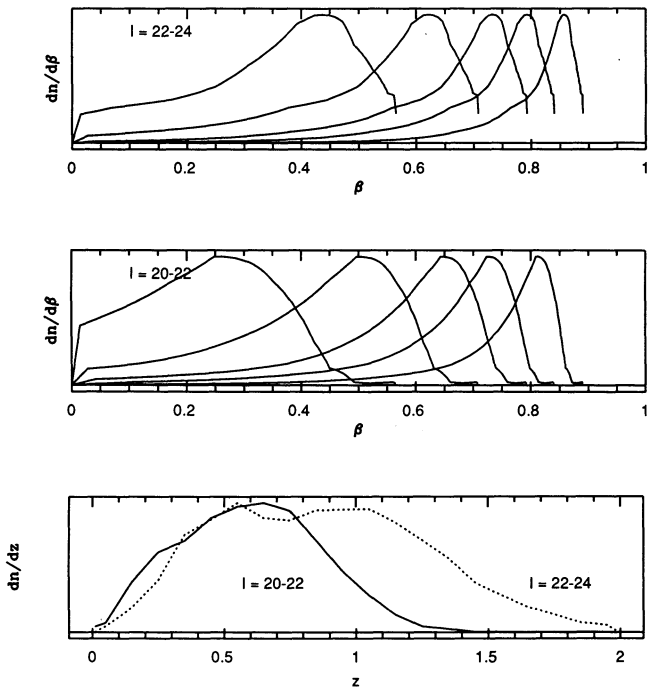

FIG. 9.—Distribution of distortion strengths for a realistic distribution of background galaxy redshifts and for various lens redshifts. The lower panel shows (*sold line*) the smoothed redshift distribution for the $I = 20$–22 CFRS redshift survey (Lilly et al. 1994) which is nearly complete and represents an increase of about an order of magnitude over previous surveys at these magnitudes (Lilly 1993; Tresse et al. 1993). The dashed curve is an extrapolation to fainter magnitudes $I = 22$–24 made assuming no evolution and kindly provided by S. Lilly. The upper panels show, for these two magnitude slices, the distribution of β values—the distortion strength relative to that for an infinitely distant object—for five lens redshifts $z_l = 0.1, 0.15, 0.2, 0.3, 0.5$, progressing from right to left. The curves move progressively to the right and become more sharply peaked as the lens redshift decreases. For $z_l \lesssim 0.2$ and for the faint magnitudes used here the β distribution is very narrow, and the single source plane approximation should be acceptable.

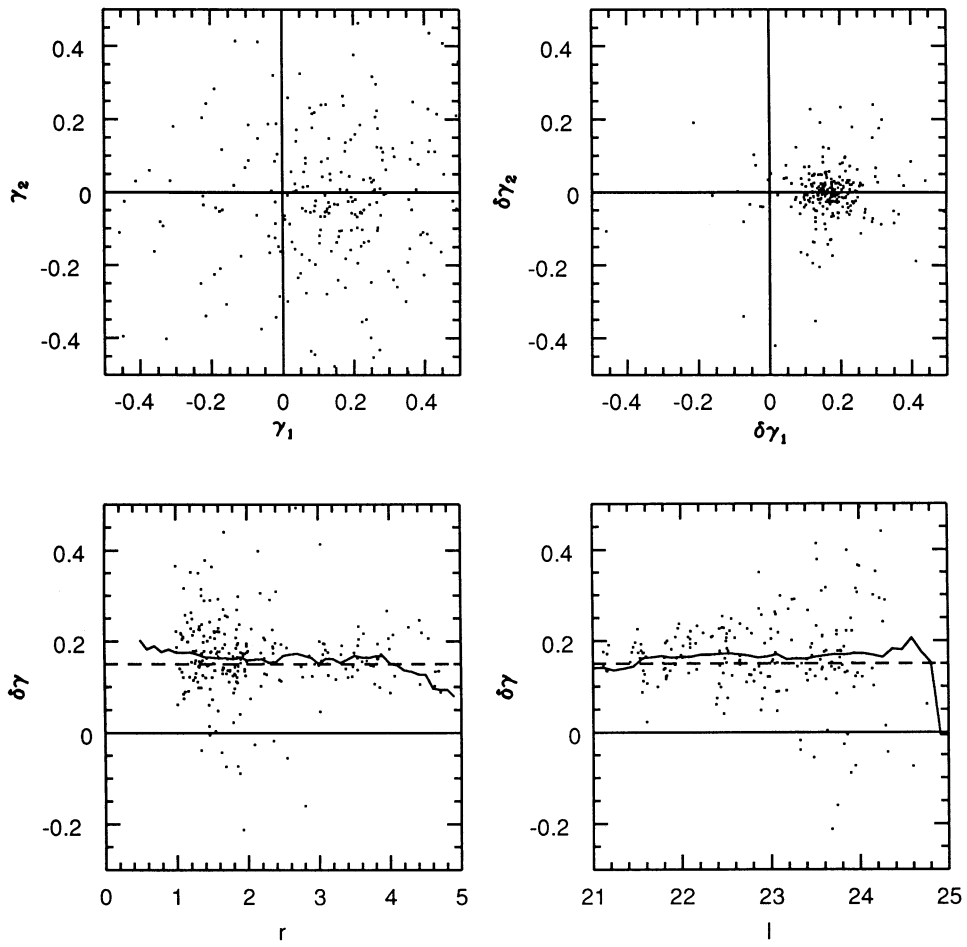

FIG. 11.—Test of shear polarizability calculation. The dashed line shows the shear applied, and the points show the individual estimates. The solid line shows a simple moving average of the shear estimates. The sample of objects analyzed here were those detected from the realistically degraded images, but the polarization was actually measured using the unsmeared images. This experiment verifies that the analytic shear polarizability does indeed correctly calibrate the raw polarization estimates.

scatter about the mean trend increases for the fainter and smaller objects. This should allow us to devise an optimal weighting scheme for combining the shear estimates, but this requires more extensive *HST* data than is currently available. Similarly, one might consider a more sophisticated weighting scheme than simply averaging the shear estimates. We have experimented with this and with other schemes such as trying to determine the mode of the polarization, but none of these has yielded significant improvement over a straight average (this is because the distribution of random polarizations is quite close to a two-dimensional Gaussian, and for a Gaussian the optimal weight is uniform).

6. SUMMARY

Images of faint galaxies are subject to two weak influences which cause their shapes to be polarized: tidal shearing of the rays as they propagate through intervening clusters and large-scale structure, and smearing with an anisotropic instrumental PSF when they reach Earth. We have described software which allows one to measure and correct for the latter to a high degree of precision and gives a quantitative estimate of the former, providing a unique and direct probe of the total mass distribution in the universe.

We have subjected the software to rigorous testing using *HST* data which are stretched to simulate lensing and then degraded to ground-based resolution and noise levels, and with an anisotropic PSF. Analyzing these data exactly as we do the ground-based data, we have shown that the correction procedure developed here appears to work very well: any residual polarization arising from PSF anisotropy is too small to detect with the small number of galaxies here. We emphasize that the correction procedure derived here is different from the techniques developed by Bonnet & Mellier (1994) and by Mould et al. (1994), but we believe we have demonstrated the validity of our method both analytically and in tests under realistic conditions.

The second main result of the paper is a demonstration of the calibration of the effect of seeing on our shear estimator. The *HST* data play a vital role here, and we have shown how the suppression depends on image size and brightness for typical observing conditions (i.e., pixel and seeing disk scale). This removes a major question mark over the calibration of

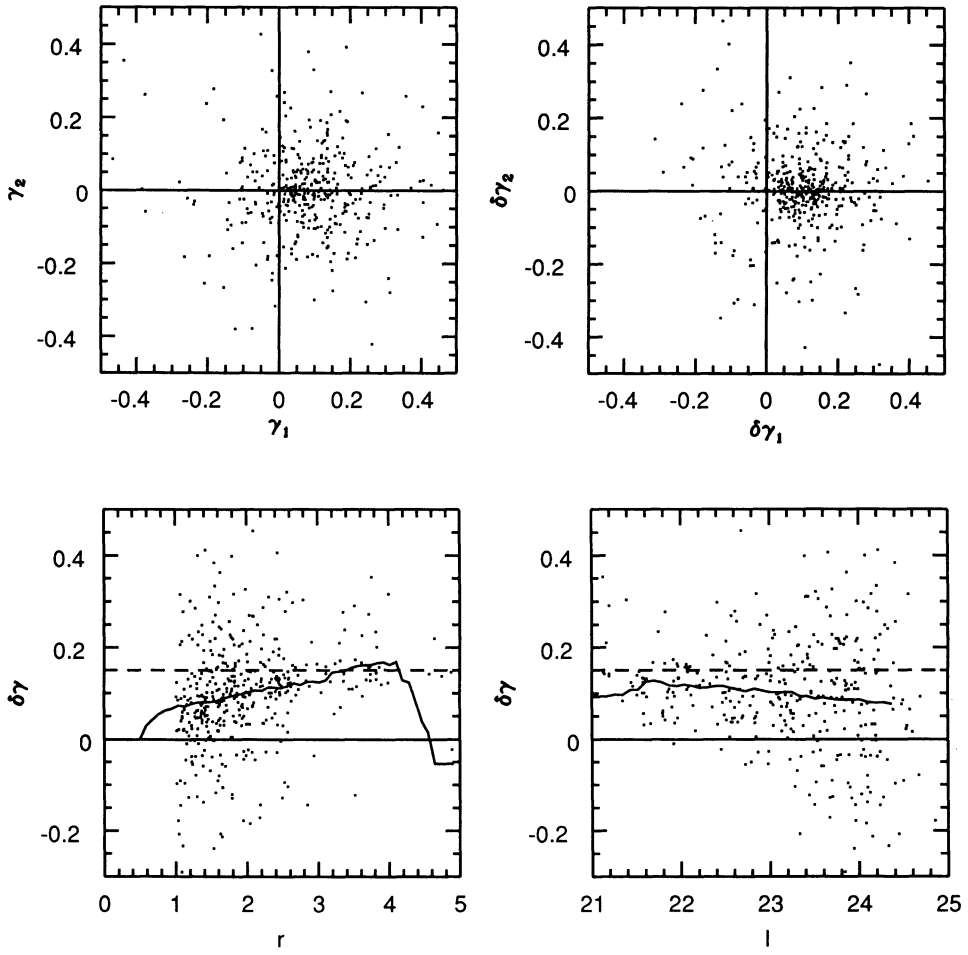

FIG. 12.—Shear estimates with FWHM = 0".5 seeing. The shear is still detected at a high level of significance but the suppression—primarily a function of image size—due to seeing can be seen. The radii here are in units of the 0".2 pixels of the rebinned images.

these observations. The limited data we use here are, we believe, sufficient to give a reasonable mean calibration for a given choice of magnitude limits. With more *HST* data we can hope to develop a detailed model for the dependence of the polarizability on size, luminosity, etc.

The work described here could usefully be extended in several respects. The polarizability tensor analysis we have developed is specific to the choice of polarization estimate (normalized to unit trace) that we have somewhat arbitrarily adopted. It would be fairly straightforward to perform the analogous calculations with polarization estimators normalized to unit determinant as suggested by Bonnet & Mellier (1994), but we have not done so. While our analysis applies for an arbitrary weighting function, the numerical results are specific to the case of a Gaussian weight and would require recalculating for any other weight function. There are a number of other parameters or features of the scheme which have been set with little serious attempt at optimization. The analytic machinery and experimental method developed here provides a quantitative way to measure the performance of any particular scheme. However, to determine the optimal point in this large parameter space will require more extensive data than are currently available. Regarding PSF anisotropy, we are confident that our procedure is adequate to remove any artificial anisotropy at the level required for mapping the mass in clusters, but we are less certain about the more ambitious goal of measuring large-scale structure, where the accuracy of the correction is more critical. Any *achromatic* PSF anisotropy can be removed, and we suspect that any residual spectrum-dependent effects are actually quite small, but a definitive calculation—which would depend on the details of the correcting optics in the telescope, the choice of filter, the statistical distribution of the spectra of stars and faint galaxies, and so on—remains to be done.

We thank Derrick Salmon, Chris Pritchet, Keith Taylor, Simon Lilly, and Greg Fahlman for many enlightening discussions.

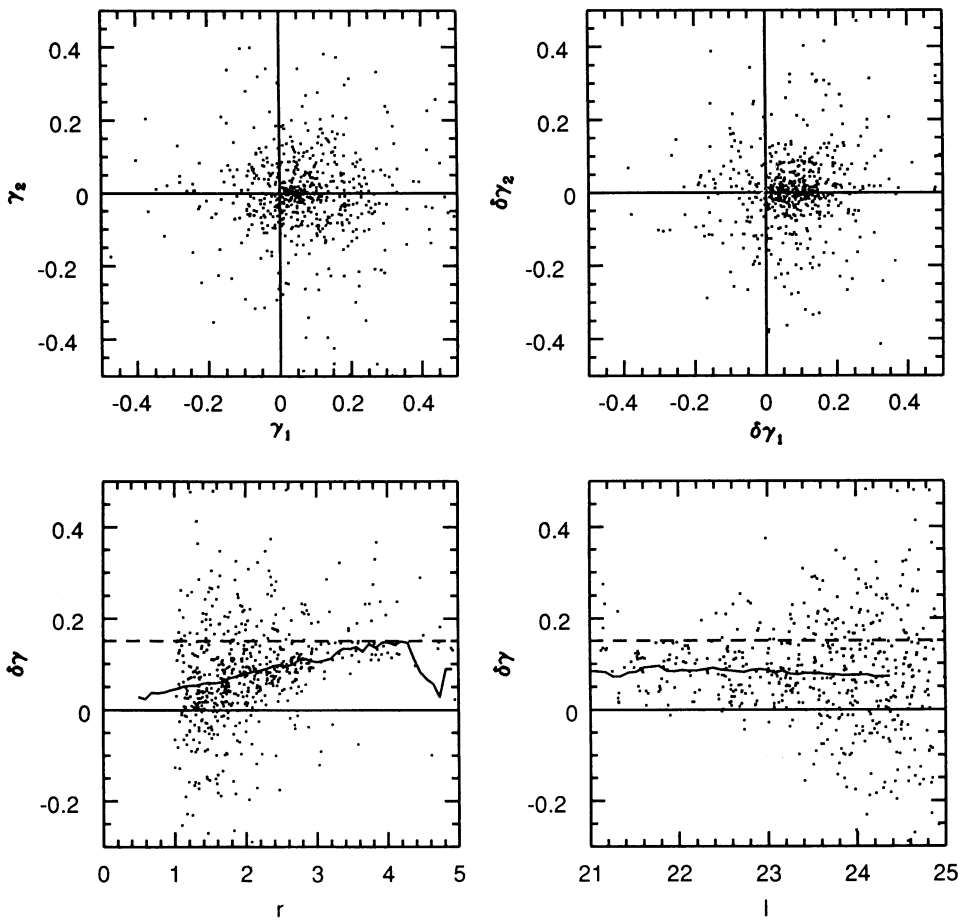

FIG. 13.—As before, but with 0.″7 seeing. The dilution is now stronger.

APPENDIX A

SMEAR POLARIZABILITY

In this section we show how the polarization of an image e_α is perturbed by anisotropy of the PSF. Using a linearized analysis (valid if the PSF is nearly circular), we derive a "polarizability" $P^s_{\alpha\beta}$ such that $\delta e_\alpha = P^s_{\alpha\beta} p_\beta$, where p_β is a measure of the PSF anisotropy.

We discuss several sources of PSF anisotropy in Appendix C. We can model the effect of all of these as a convolution of the post-seeing circularly smeared image with a small, normalized, but highly anisotropic PSF:

$$f'(\boldsymbol{\theta}) = \int d^2\theta' g(\boldsymbol{\theta}') f(\boldsymbol{\theta} - \boldsymbol{\theta}') \,. \tag{A1}$$

This is obviously true for wind-shake and other effects arising in the telescope, but is also valid for, e.g., atmospheric dispersion, which happens at the same time as the circular smearing, due to fact that convolutions commute.

We can set the spatial origin so that the first moment of g vanishes, and we find that on Taylor expanding f, the weighted quadrupole is perturbed according to

$$Q'_{ij} \equiv \int d^2\theta W(\theta)\theta_i\theta_j f'(\boldsymbol{\theta}) = Q_{ij} + \delta Q_{ij} = Q_{ij} + q_{lm}\mathscr{Z}_{lmij} \,, \tag{A2}$$

where

$$q_{lm} \equiv \int d^2\theta\theta_l\theta_m g(\boldsymbol{\theta}) \,, \tag{A3}$$

and where

$$\mathscr{Z}_{lmij} = \int d^2\theta\, W(\theta)\theta_i\,\theta_j f_{,lm}(\boldsymbol{\theta}) = \int d^2\theta f(\boldsymbol{\theta}) z_{lmij}\,, \tag{A4}$$

where we have integrated by parts twice and we have defined

$$z_{lmij} = \frac{\partial[W(\theta)\theta_i\,\theta_j]}{\partial\theta_i\,\partial\theta_m}\,. \tag{A5}$$

The simplest case is $W = 1$, in which case we have

$$z_{lmij} = \delta_{il}\,\delta_{jm} + \delta_{jl}\,\delta_{im}\,. \tag{A6}$$

In the general case,

$$z_{lmij} = W(\delta_{il}\,\delta_{jm} + \delta_{jl}\,\delta_{im}) + 2W'(\delta_{im}\,\theta_j\theta_l + \delta_{jm}\,\theta_i\theta_l + \delta_{il}\,\theta_j\theta_m + \delta_{jl}\,\theta_i\theta_m + \delta_{lm}\,\theta_i\theta_j) + 4W''\theta_i\theta_j\theta_l\theta_m\,, \tag{A7}$$

where prime denotes differentiation with respect to θ^2.

The trace of q_{ij} will change the size of the image, but not the shape, so we take q_{ij} to be trace free and, of course, symmetric:

$$\begin{pmatrix} q_{11} & q_{12} \\ q_{21} & q_{22} \end{pmatrix} = \frac{1}{2}\begin{pmatrix} p_1 & p_2 \\ p_2 & -p_1 \end{pmatrix}, \tag{A8}$$

which defines the PSF anisotropy vector p_α.

From the definition of the polarization (eq. [3.2]) in terms of Q_{ij} and using equation (A2), we have, to linear order in p_α,

$$\delta e_\alpha = P^s_{\alpha\beta}\,p_\beta\,, \tag{A9}$$

with

$$P^s_{\alpha\beta} = X^s_{\alpha\beta} - e_\alpha e^s_\beta\,, \tag{A10}$$

where

$$X^s_{\alpha\beta} = \frac{1}{T}\int d^2\theta \begin{bmatrix} 2W + 4W'\theta^2 + 2W''(\theta_1^2 - \theta_2^2)^2 & 4W''(\theta_1^2 - \theta_2^2)\theta_1\,\theta_2 \\ 4W''(\theta_1^2 - \theta_2^2)\theta_1\,\theta_2 & 2W + 4W'\theta^2 + 8W''\theta_1^2\,\theta_2^2 \end{bmatrix} f(\boldsymbol{\theta})\,, \tag{A11}$$

and with

$$e^s_\alpha \equiv \frac{1}{T}\int d^2\theta \begin{pmatrix} \theta_1^2 - \theta_2^2 \\ 2\theta_1\,\theta_2 \end{pmatrix} (6W' + 2W''\theta^2) f(\boldsymbol{\theta})\,. \tag{A12}$$

We can use equation (A9) as follows. From the observed stellar e, s,—which, being circular, will have diagonal $P^s_{\alpha\beta}$—we can infer p_α (as a function of position on the chip if necessary). Having fitted the stellar ellipticities to some reasonable model, we can then use equation (A9) to calculate the necessary linear correction to the galaxy ellipticity. This restores the polarization values to what they would have been for an observer with a perfectly circular PSF.

One could make some simplifications here: the expectation values of the off-diagonal terms in $X^s_{\alpha\beta}$ vanish for randomly oriented objects, as does the difference between diagonal terms, and we have, for the shift in the mean polarization,

$$\langle \delta e_\alpha \rangle = P^s p_\alpha\,, \tag{A13}$$

with

$$P^s = \frac{\int d^2\theta(2W + 4W'\theta^2 + W''\theta^4) f(\boldsymbol{\theta})}{\int d^2\theta W\theta^2 f(\boldsymbol{\theta})} - \frac{\langle e_\alpha e^s_\alpha \rangle}{2}\,. \tag{A14}$$

Thus, if we simply use this reduced scalar polarizability and apply the correction $\delta e_\alpha = -P^s p_\alpha$, then we make no error *on average*, though with a finite number of galaxies the precision of the correction should be better if we use the full polarizability tensor, and this is what we do.

The smear polarizability depends on both the weight function and on the galaxy shape. With our detection and analysis scheme, the weight function scale length is derived from the actual image shape, and one can then see on dimensional grounds from equations (A11) and (A12) and from the definition of the trace T that $P^s_{\alpha\beta}$ scales inversely as the area of the image.

APPENDIX B

SHEAR POLARIZABILITY

In this section we attempt to calculate how the polarization values change under the influence of a small, coherent gravitational shear. This is superficially very similar to the calculation of Appendix B, and the goal is to calculate some kind of "shear-polarizability" which provides a calibration factor to convert raw polarization values to shear estimates. As before, the result

depends on the details of the weighting function $W(\theta)$ and on the shapes of the galaxy, but the situation is much more difficult here if the galaxies are only poorly resolved, since the polarizability depends on the shapes of the galaxies before seeing which is not measurable. Here we will calculate the shear polarizability in the limit that seeing can be neglected. For ground-based images this will not be a very good approximation, but it provides a starting point.

The perturbation to the surface brightness pattern due to gravitational lensing is

$$f'(\theta_i) = f(\theta_i - \phi_{,ij}\theta_j) , \tag{B1}$$

where perturbed angles are understood to be measured relative to the perturbed centroid position and where ϕ is the surface potential.

If we take $\phi_{,ij}$ in equation (B1) to be small and effectively constant over the size of the background galaxy, then on substituting in equation (3.1) we have

$$Q'_{ij} = Q_{ij} - \phi_{,lm}\int d^2 W(\theta)\theta_i\theta_j\theta_m \partial f(\boldsymbol{\theta})/\partial\theta_l , \tag{B2}$$

or, on integrating by parts,

$$Q'_{ij} = Q_{ij} + \phi_{,lm} Z_{lmij} , \tag{B3}$$

with

$$Z_{lmij} = \int d^2\theta z_{lmij} f(\boldsymbol{\theta}) , \tag{B4}$$

where

$$z_{lmij} = \frac{\partial[W(\theta)\theta_i\theta_j\theta_m]}{\partial\theta_l} = W(\delta_{il}\theta_j\theta_m + \delta_{jl}\theta_i\theta_m + \delta_{ml}\theta_i\theta_j) + 2W'\theta_l\theta_m\theta_i\theta_j , \tag{B5}$$

and where, as before, prime denotes differentiation with respect to θ^2.

Now the perturbation to the polarization is, from equation (3.2),

$$\delta e_\alpha = \frac{\delta Q_\alpha}{T} - e_\alpha\frac{\delta T}{T} . \tag{B6}$$

Writing

$$\phi_{,ij} = \begin{pmatrix} \kappa+\gamma_1 & \gamma_2 \\ \gamma_2 & \kappa-\gamma_1 \end{pmatrix} , \tag{B7}$$

with κ the dimensionless surface density and γ the shear, we find

$$\delta Q_{ij} = (\kappa+\gamma_1)Z_{11ij} + (\kappa-\gamma_1)Z_{22ij} + 2\gamma_2 Z_{12ij} . \tag{B8}$$

Calculating the first-order change in e_α using equation (3.2), we find a large number of terms. Some of these involve the surface density κ, which might seem surprising. These terms arise from the first-order perturbation to the trace T. However, the expectation value for these terms taken over the randomly oriented (to zeroth order) background galaxies vanishes, and we therefore ignore them without fear of introducing a bias. The remaining terms are linear in γ_α:

$$\delta e_\alpha = P^\gamma_{\alpha\beta}\gamma_\beta , \tag{B9}$$

with

$$P^\gamma_{\alpha\beta} = X^\gamma_{\alpha\beta} - e_\alpha e^\gamma_\beta , \tag{B10}$$

where $P^\gamma_{\alpha\beta}$ defines the *shear polarizability* which is quite analogous to the smear polarizability defined in Appendix A, but now with somewhat different moments

$$X^\gamma_{\alpha\beta} = \frac{1}{T}\int d^2\theta \begin{bmatrix} 2W\theta^2 + 2W'(\theta_1^2-\theta_2^2)^2 & 4W'(\theta_1^2-\theta_2^2)\theta_1\theta_2 \\ 4W'(\theta_1^2-\theta_2^2)\theta_1\theta_2 & 2W\theta^2 + 8W'\theta_1^2\theta_2^2 \end{bmatrix} f(\boldsymbol{\theta}) , \tag{B11}$$

$$e^\gamma_\alpha \equiv 4e_\alpha + \frac{2}{T}\int d^2\theta \begin{pmatrix} \theta_1^2-\theta_2^2 \\ 2\theta_1\theta_2 \end{pmatrix} \theta^2 W' f(\boldsymbol{\theta}) . \tag{B12}$$

Note that while the smear polarizability scales inversely as the area of the object, the shear polarizability is a function only of the shape of the image.

As with the smear polarizability, one can calculate a scalar polarizability which gives the shift in the mean polarization for intrinsically randomly oriented objects. If we average over an ensemble of galaxies with the same shape but random orientations, we find

$$\langle e_\alpha\rangle = P^\gamma\gamma_\alpha , \tag{B13}$$

where

$$P^\gamma = 2 + \frac{\int d^2\theta W' \theta^4 f(\theta)}{\int d^2\theta W \theta^2 f(\theta)} - \langle e_\alpha e_\alpha^\gamma \rangle \,, \tag{B14}$$

so a fair estimate of the shear γ_α is given by taking the mean of e_α/P^γ. However, as with the smear polarizability, there is more information in the full polarizability tensor, so this is what we use.

APPENDIX C

ARTIFICIAL SOURCES OF ANISOTROPY

Weak lensing allows the possibility of measuring fluctuations on large scales, but only if the precision can be kept close to the minimum uncertainty implied by the statistically random intrinsic background galaxies. It is therefore useful to consider what systematic effects might arise in order than these can be minimized or corrected for.

Many of the effects consist of a unidirectional smearing of the images; in the absence of seeing, each image would then be a line of half-length $\delta\theta$, and the PSF anisotropy parameter as defined in equation (A8) is then $p_\alpha = \int d^2\theta g \theta^2 / \int d^2\theta g = \delta\theta^2/3$. The size of the effect on our shear estimates depends on the size of the galaxy images. For the degraded *HST* data used here (smeared to $\simeq 0''.5$ seeing and with $0''.2$ pixels) we find a median smear-polarizability $P^m \sim 0.45$ (pixels)$^{-2}$, so the typical induced polarization is

$$\delta e_\alpha \simeq 3.75(\delta\theta/1'')^2 \,, \tag{C1}$$

so smearing with a boxcar PSF of half-width $0''.1$, say, would induce a polarization of $\simeq 4\%$. In comparison, the expected signal from large-scale structure is at about the $\sim 1\%$ level. With an idea then of what size of effect might be tolerated, we will now survey some of the obvious sources of PSF anisotropy.

C1. ATMOSPHERIC REFRACTION

Refraction by the atmosphere shifts images according to

$$z_a = z_t - R(z_a, \lambda) \,, \tag{C2}$$

where z_a and z_t are the apparent and real zenith distances, and the deflection angle $R(z, \lambda)$ is tabulated in Allen (1973). For reasonably small zenith angles,

$$R \simeq R_0(\lambda) \tan z \,, \tag{C3}$$

where $R_0 \simeq 60''$ at sea level and at optical wavelengths, falling to $R_0 \simeq 35''$ at a 4000 m site such as Mauna Kea. The deflection angle is a fairly weak function of wavelength: $d \log R/d \log \lambda \simeq \{7.9\%, 4.5\%, 3.2\%, 1.9\%\}$ at wavelengths {4500, 5500, 7000, 9000 Å} corresponding to *B*, *V*, *R*, and *I* wavebands.

The *stretching* of images due to the atmospheric refraction gives an apparent shear

$$2\gamma = dR/dz_a \simeq R_0 z_a^2/6 \simeq 3 \times 10^{-5} z_a^2 \,, \tag{C4}$$

which is entirely negligible for reasonable zenith angles for the signals of interest. In fact, the shear rises to only about 1% at $\sim 5°$ above the horizon.

There is, however, the possibility for this effect to introduce a systematic anisotropic smearing in systems where the guide star lies at a considerable angle from the CCD (at CFHT the angle is $\simeq 0°.5$–$1°$). In a very long integration the position of objects on the CCD will then drift by an angle $\sim 0''.12\,\Delta(z^2)$. This effect can easily be avoided by keeping the exposures reasonably short (which tends to be desirable for other reasons). In any case, the effect is to produce an essentially achromatic smearing which is constant over the frame which can then be removed using the technique described in Appendix A.

C2. ATMOSPHERIC DISPERSION

Atmospheric dispersion is potentially a more worrying problem. The atmosphere, acting as a prism, will disperse any continuum emission over an angle

$$\delta\theta \sim (\delta\lambda/\lambda) R \, d\ln R/d\ln\lambda \,, \tag{C5}$$

where the first factor is the half-width of the filter. For *I*-band observations we find $\delta\theta \simeq 0''.12z$, giving a polarization shift

$$\delta e \sim 0.05 z_a^2 \,. \tag{C6}$$

This is quite a large effect. More worrisome, the effect depends on the spectrum of the object. We measure the PSF anisotropy from stars which are continuum objects, but then we apply the correction to galaxies. The worst case would be a galaxy dominated by a single very strong emission line which would then be undispersed, and our "correction" would then actually introduce a systematic error. For less extreme objects and for realistic filters, the dependence of image profiles on the object spectra is rather weak; the galaxies and the stars may have systematically different spectral slopes, but to first order a change in the slope of the spectrum simply displaces the centroid of the object without changing the shape of the PSF. To change the shape of the image requires there

to be a change in the slope of the spectrum over the typically rather narrow passband of the filter. For normal spectra, any such effect is therefore quadratic in the filter width and is quite small. Note, however, that these problems would be exacerbated if one tried to stack images taken in different passbands.

A quantitative estimate of the strength of this effect for realistic galaxy/stellar spectral energy distributions remains to be done, but as the effect is quadratic in zenith angle and prevention is better than the cure, the obvious solution is to try to keep to a smal zenith angle if at all possible. Another possibility is to employ an atmospheric dispersion compensator.

C3. GUIDING ERROR

One unavoidable effect is guiding error. This will typically contain a systematic effect and a stochastic effect (from wind-shake for example). Any such effects are however achromatic and constant across the CCD and (provided they are not too large) can readily be corrected for.

C4. OPTICAL ABERRATION

This effect is highly site dependent. Spot diagrams for the Canada-France-Hawaii Telescope (CFHT) (kindly provided by Derrick Salmon at CFHT) show that, according to the design specifications of the wide field corrector, the aberration should be quite small for the FOCAM detector—a single chip at the center of the very wide (50′) corrected field of view—and also for devices such as MOCAM, so insofar as the aberration is achromatic, the linearized correction developed here should work. Eventually, we can expect that the whole of the ~ 1 square degree corrected field will be tiled with chips, and the aberration increases considerably toward the edge of the corrected field, so this may become more of an issue. The spot diagrams show the distortion of the images to be fairly achromatic, but there is some color dependence; however, as with atmospheric dispersion more work is needed to quantify the effect. Note that even if the PSF does vary considerably for stars as opposed to galaxies, there may be some remedy. If the effect is repeatable (e.g., a simple function of distance from the axis of the telescope), then it may be possible to directly measure any systematic over- or undercorrection and modify the correction appropriately. Another way to remove repeatable PSF anisotropy is to rotate the instrument by $\pi/2$ between exposures. Even if the effects are not repeatable, if they vary slowly across the field, then as one will have a very large number of stars it may prove possible to develop a model for the PSF as a function of color. Finally, if all else fails, it may prove necessary to work with narrower band filters, though this entails some overhead.

One interesting effect we have come across at CFHT was a reproducible linear gradient of ellipticity across the CCD frame. The cause of this is suspected to have been an asymmetric aberration of the primary mirror. This is known to cause a PSF anisotropy which changes sign as the chip is moved up and down during the focusing, and we may well have been seeing a slight misalignment of the chip and focal plane coupling to this and generating a gradient in image polarization.

C5. IMAGE ADDITION

Even under perfect observing conditions, some PSF anisotropy will inevitably arise from stacking multiple images. We have done this using only linear translations and with integer pixel shifts, and this can easily introduce spurious polarization at the few percent level. The effect is achromatic and slowly varying and should therefore be correctable. It is possible to apply fractional pixel shifting with some interpolation scheme, but this does not really avoid the problem. An often quoted advantage of "sinc-interpolation" is that it preserves the lack of correlation in the photon counting noise. It does not, however, preserve the shape of signals, and it does introduce PSF anisotropy.

This effect can be more dangerous if one tries to stack images which are rotated with respect to each other. One then obtains a moire pattern, and the induced polarization will then vary periodically with a high spatial frequency. With the limited number of stars it may be difficult or impossible to map this pattern, and the correction will then fail.

REFERENCES

Allen, C. W. 1973, Astrophysical Quantities (London: Athlone)
Blandford, R. D., Saust, A. B., Brainerd, T. G., & Villumsen, J. V. 1991, MNRAS, 251, 600
Bonnet, H., Fort, B., Kneib, J.-P., Mellier, Y., & Soucail, G. 1994, A&A, 280, L7
Bonnet, H., & Mellier, Y. 1994, A&A, in press
Broadhurst, T., Taylor, A., & Peacock, J. 1994, MNRAS, in press
Cuillandre, J. C., Mellier, Y., Crampton, D., Murowinski, R., & Arsenault, R. 1994, IAU Symp. 167, ed. A. G. Davis Philip (Dordrecht: Reidel), in press
Dahle, H., Maddox, S. J., & Lilje, P. B. 1994, preprint
Fahlman, G., Kaiser, N., Squires, G., & Woods, D. 1994, ApJ, 437, 56
Fort, B., & Mellier, Y. 1994, A&A Rev., in press
Gould, A., & Villumsen, J. 1994, ApJ, 428, L45
Jarvis, J. F., & Tyson, J. A. 1981, AJ, 96, 476
Kaiser, N. 1992, ApJ, 388, 272
Kaiser, N., & Squires, G. 1993, ApJ, 404, 441 (K593)
Kaiser, N., Squires, G., Fahlman, G., & Woods, D. 1994, Proc. of Meribel Conf. on Clusters of Galaxies, in press
Kochanek, C. S. 1991, ApJ, 382, 58
Kron, R. G. 1980, ApJS, 43, 305
Lilly, S. J. 1993, ApJ, 411, 501
Lilly, S. J., Le Fevre, O., Hammer, F., Cranston, D., & Tresse, L. 1994, in Proc. 35th Herstmonceux Conf., ed. S. Maddox, in press
Luppino, G., Bredthauer, & Geary, 1994, preprint
Mellier, Y., Fort, B., Bonnet, H., & Kneib, J.-P. 1994, in Cosmological Aspects of X-Ray Clusters of Galaxies, ed. W. Seitter et al., in press
Miralda-Escude, J. 1991a, ApJ, 370, 1
———. 1991b, ApJ, 380, 1
Mould, J., Blandford, R., Villumsen, J., Brainerd, T., Smail, I., Small, T., & Kells, W. 1994, MNRAS, in press
Schneider, S. 1994, preprint
Schneider, S., & Seitz, C. 1994, preprint
Schramm, T., & Kayser, R. 1994, preprint
Seitz, C., & Schneider, S. 1994, preprint
Smail, I., Ellis, R. S., Fitchett, M. J., & Edge, A. C. 1994a, MNRAS, in press
———. 1994b, MNRAS in press
Tresse, L., Hammer, F., Le Fevre, O., & Proust, D. 1993, A&A, 277, 53
Tyson, J. 1995, Proc. of Les Houches Summer School (New York: Elsevier)
Tyson, J., Valdes, F., & Wenk, R. 1990, ApJ, 349, L19
Yee, H. K. C. 1991, PASP, 103, 396

PLATE 8

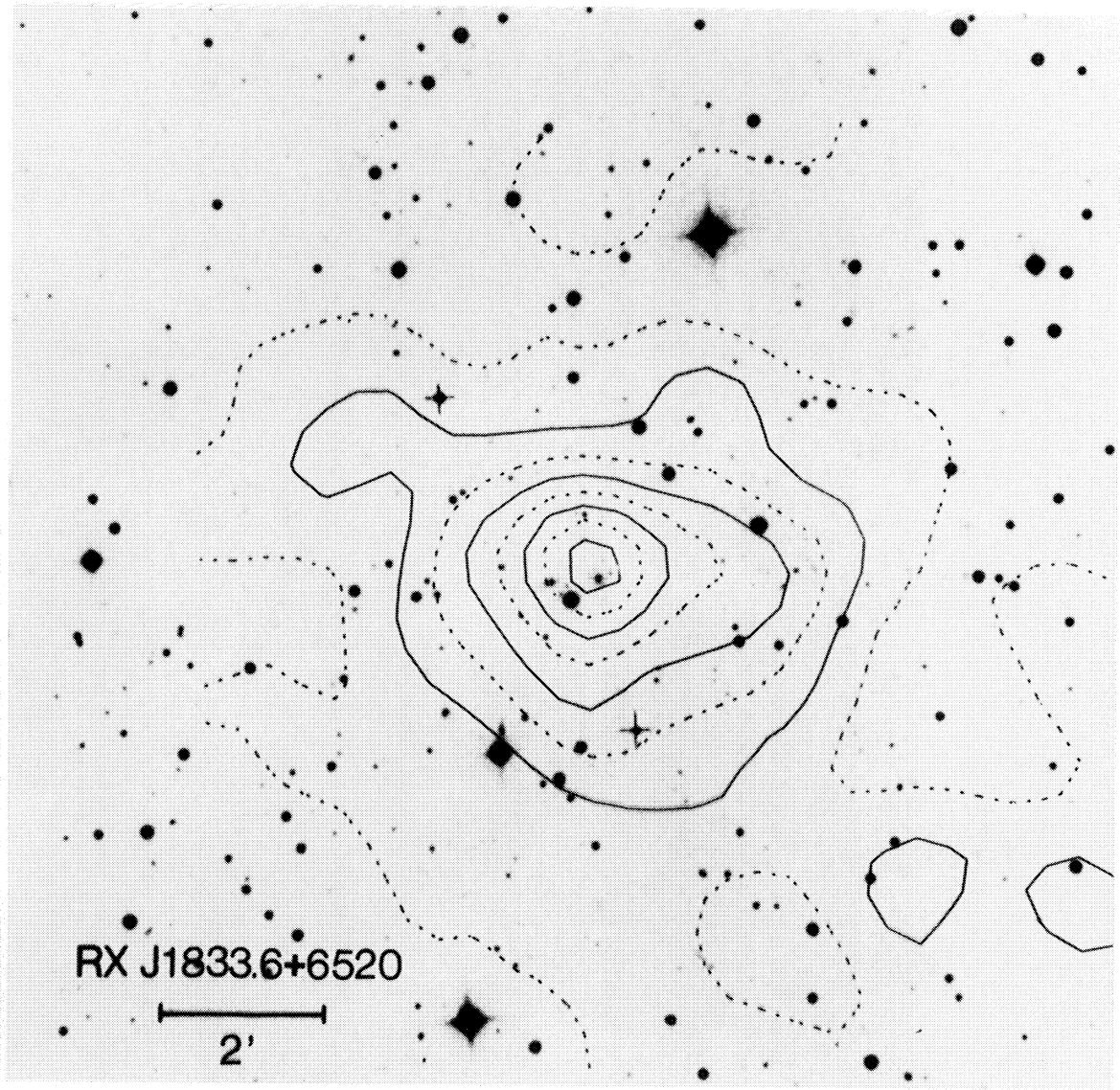

FIG. 1*h*

HENRY et al. (see 449, 423)

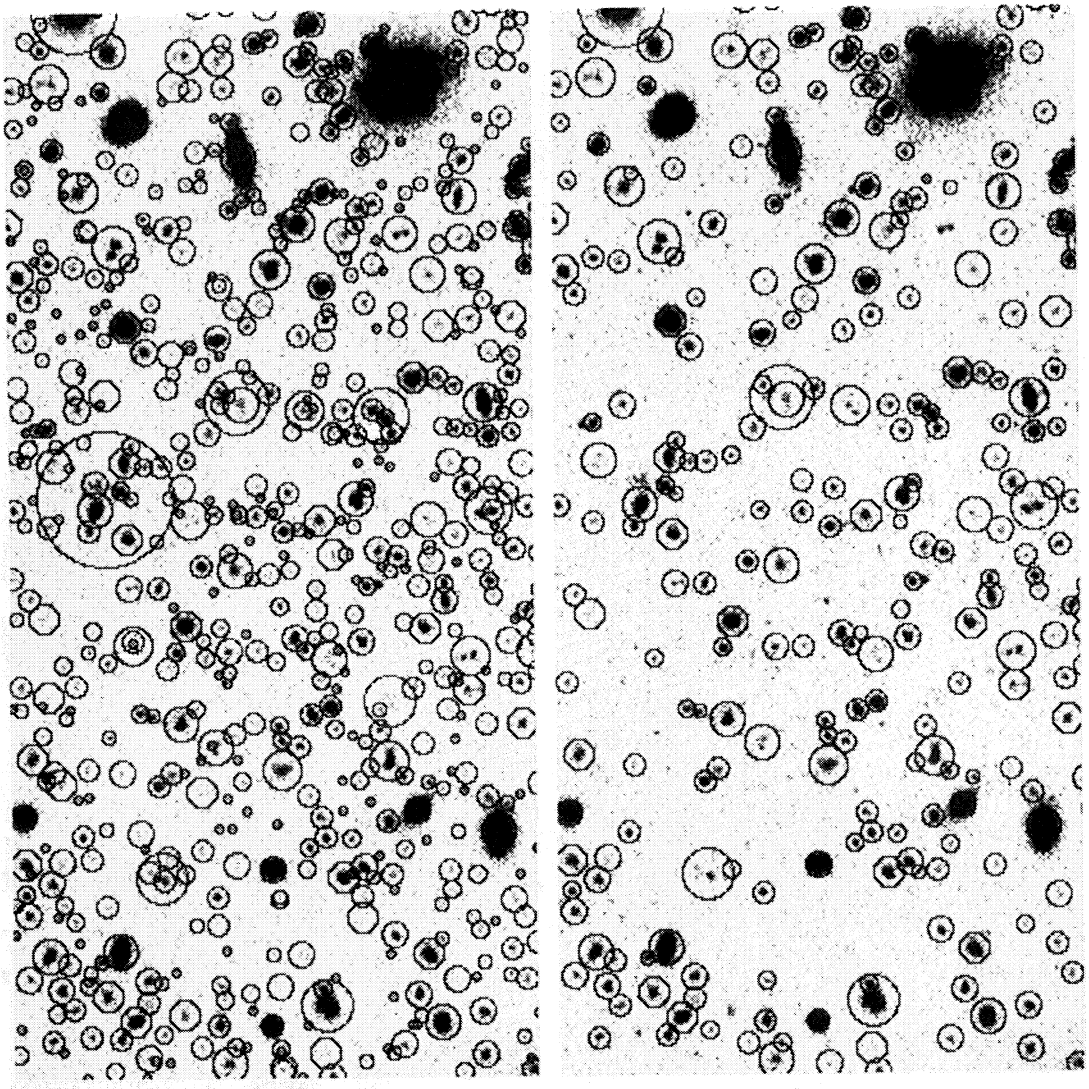

FIG. 3.—Hierarchical peak finding in two dimensions. The panel on the left shows the raw output of the peak finder. The image underlaid here is a small fragment of the "avsigclip" sum of 10 20-minute V-band exposures taken at the NTT with 0".7 FWHM seeing and with 0".34 pixels. The 256 × 512 pixel subimage shown here lies a few arcminutes off the centre of A1689. Most of the obvious real objects are detected, but so are a large number of (typically very small) noise peaks and a few apparent groups, etc. The panel on the right shows the result of applying a spatial coincidence test between the raw catalog shown on the left and a catalog constructed from a similarly deep I-band image of the same field. Most of the small noise peaks have gone, as have most of the composite objects. We also lose a few significant (in V) but extremely blue objects. The effective limiting magnitude in the final catalog is around $I = 25$, and there are about 70 objects per square arcminute.

PLATE 10

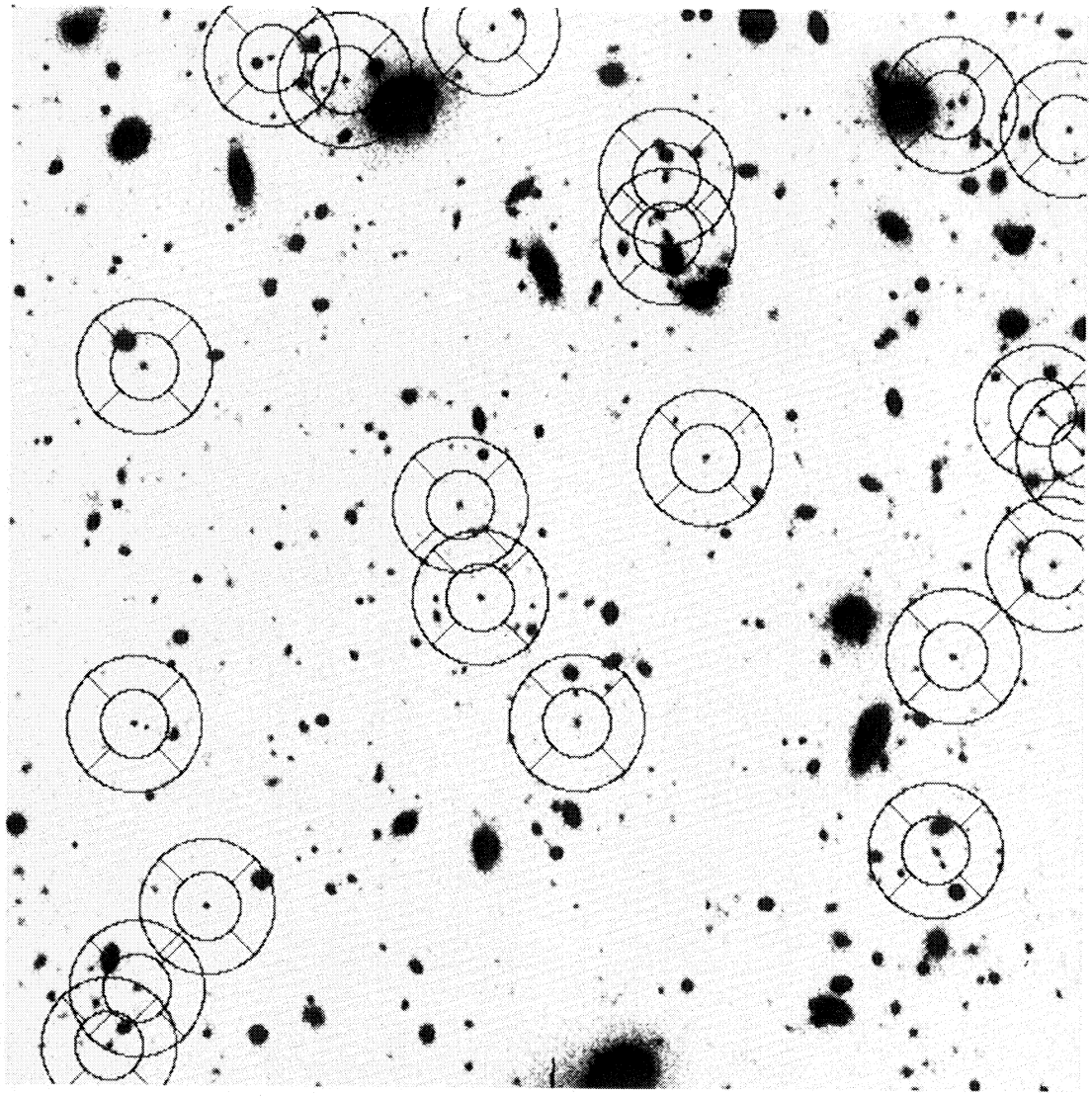

FIG. 4.—To determine the local sky level in the vicinity of an object we first determine the modal sky value in four sectors surrounding the object. We then fit a bilinear model to these values. The sectors are illustrated for a subsample of the objects detected from the NTT data. This step is optional.

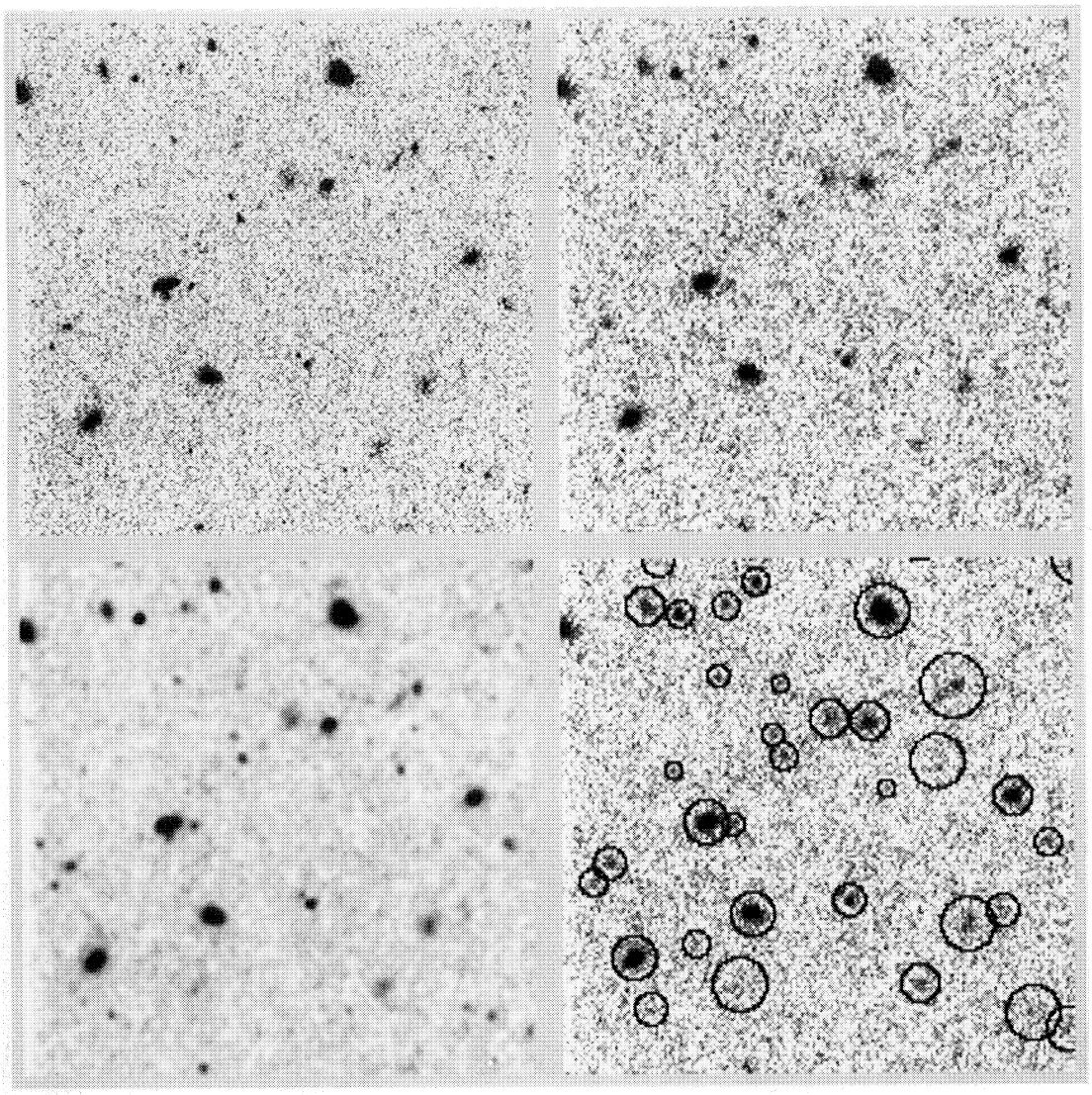

FIG. 6.—On the upper left is shown roughly a quarter of a single WFPC2 field (380 × 380 pixels at 0.″1 per pixel), and below it the result of smoothing this to simulate 0.″5 seeing and rebinning to 0.″2 pixels. This is a three-orbit *I*-band integration. In the upper right-hand panel we have added noise to the level appropriate for a similar length integration on a telescope like the CFHT or the NTT. For each field, two such degraded images (with independent realizations of noise) were analyzed in exactly the same way that we analyze the real ground-based data, and the chart on the lower right shows the result of the object finding after spatial coincidence testing. The final density of objects is very similar to those found in the NTT data shown above.

KAISER, SQUIRES, & BROADHURST (see 449, 465)

PLATE 12

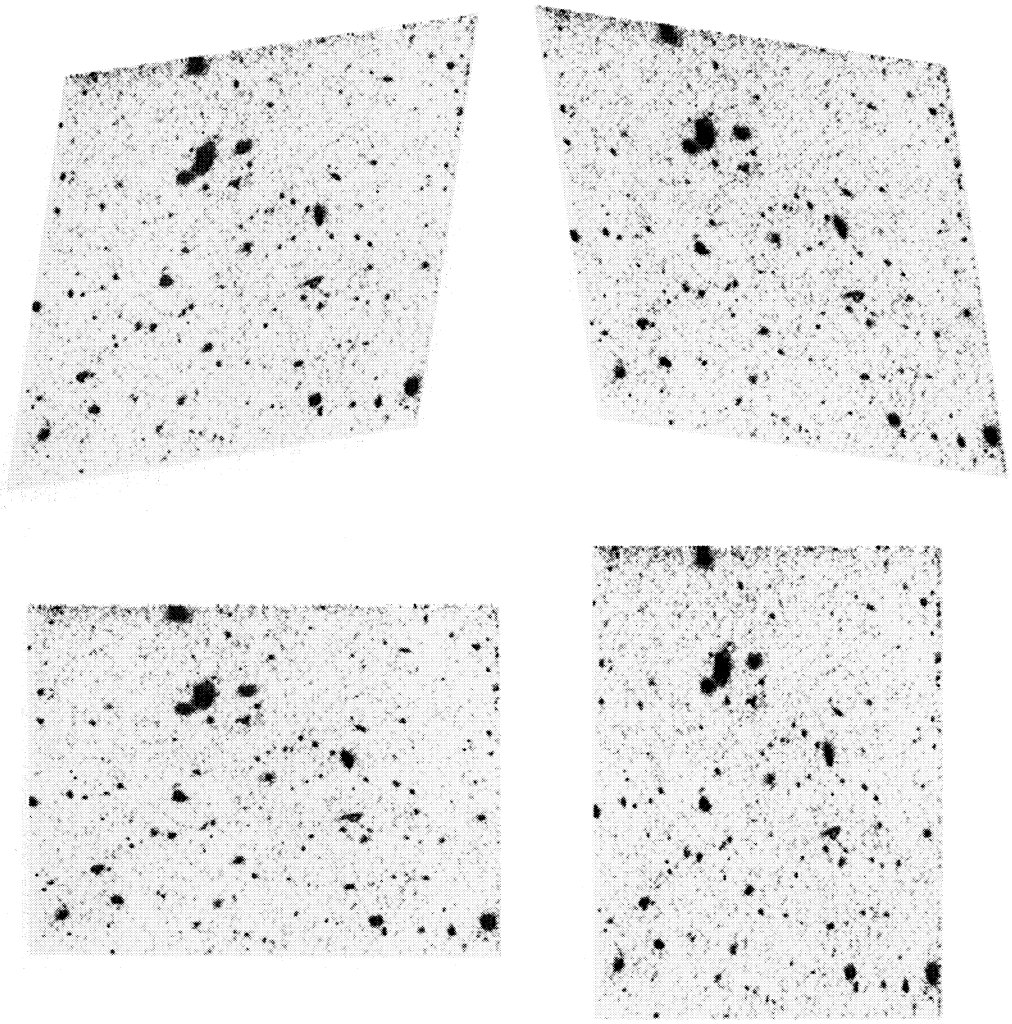

FIG. 10.—Artificially sheared *HST* images. The original image here was a single WFPC2 CCD field, and a shear of 15% was applied to the CCD images in four directions as shown. In total, three frames like this were used.

KAISER, SQUIRES, & BROADHURST (see 449, 468)